Studying Eclipse-like Behaviour in Two AGN: NGC 6814 and Zw 229.015

by

Ben Anthony Pottie

A Thesis Submitted to Saint Mary's University, Halifax, Nova Scotia in Partial Fulfillment
of the Requirements for the Degree of Master of Science in Astronomy
(Department of Astronomy and Physics)

2024, Halifax, Nova Scotia

Approved: _____

Dr. Luigi Gallo (Supervisor)

Approved: _____

Dr. Roby Austin (Committee Member)

Approved: _____

Dr. Ian Short (Committee Member)

Date: August 29, 2024.

Acknowledgements

I wish to thank Dr. Luigi Gallo for his supervision over the past three years, and for how he has helped shape me as a researcher and scientist. I would also like to give my thanks to the SMASHERS research group, especially Adam Gonzalez, for their help in my research over the years, and to my amazing girlfriend, Riana, for her support and help with stress.

I would also like to extend thanks to the anonymous MNRAS referee for their comments on the original manuscript for our paper "A Colourful Analysis: Probing the Eclipse of the Black Hole and Central Engine in NGC 6814 Using X-ray Colour-Colour Grids", as well as to Dr. Roby Austin and Dr. Ian Short for taking the time to be a part of my committee.

Contents

List of Figures

List of Tables

Abstract

Studying Eclipse-like Behaviour in Two AGN: NGC 6814 and Zw 229.015

by Ben Pottie

Studying transient events in active galactic nuclei (AGN) can provide useful information about the AGN environment. In this work, transient-like events in NGC 6814 and Zw 229.015 were studied. Colour-colour grids, which provide better time resolution than spectral analysis and can break model degeneracies, were applied to the eclipse data for NGC 6814. These grids revealed a complex multi-cloud geometry for the obscurer, dismissing the original idea of a single, homogeneous cloud. In Zw 229.015, flux-resolved spectral analysis was used to study a concurrent dip in both the UV and X-ray light curves. The analysis attributed the likely source of the flux dip to continuum changes through either coronal variability or accretion rate changes. Timescale consideration revealed thermal processes to be the source of the variability causing the dip. Separate analyses of two different AGN showing similar transient-like behaviour, require different explanations.

August 29, 2024

Chapter 1

Introduction

At the center of most galaxies exists a supermassive black hole (SMBH) with masses ranging from millions to billions of solar masses. A small number of these galaxies are considered active and classified as active galactic nuclei (AGN). When active, the SMBHs in these galaxies are undergoing accretion. This is the process by which matter falls onto a gravitational body, resulting in the conversion of gravitational potential energy into radiation (Gallo 2011).

In a normal galaxy, the light we see is dominated by the stellar processes occurring within. Active galaxies are instead dominated by light from the processes occurring within the central regions, which can produce some of the highest luminosities in the Universe. Even though the SMBH tends to only make up about 0.3% of the total stellar mass, it dominates the light we see from active galaxies. This light can extend

over the entire electromagnetic spectrum, but is seen to be especially variable in the X-ray band. X-ray emission also comes from regions close to the SMBH, so studying X-ray emission from AGN provides us with significant information about the central region (Gallo 2011).

Due to the differences in the dominant emission processes between active galaxies and normal galaxies, there are also large differences in the appearances of their spectra. Since normal galaxies are dominated by the collective emission of all the contained stars, their emission tends to follow a blackbody shape. In active galaxies, the emission has a power-law dominated shape (with the slope quantified by the photon index parameter, Γ) (Gallo 2011).

1.1 The AGN SED and Unification Model

1.1.1 AGN SED and Components

The components that make up AGN are the central engine (consisting of the SMBH and accretion disc), a hot electron corona, a dusty torus, the broad-line region (BLR), and the narrow-line region (NLR) (Figure 1.1). Each of these components can contribute to AGN spectra from radio to X-rays (Figure 1.2). The central engine occupies the innermost region, with the corona configured in some "lamppost" geometry at some height, z, above the black hole/inner disc and displaced some distance, x, from the

black hole spin axis (Figure 1.3). The inner region is on the order of light-hours across. Located light-weeks to light-months from the central region is the BLR, which is also interior to the dusty torus. At parsec scales, the accretion disc transitions into the dusty torus, which occupies the same plane as the disc. Exterior to the torus, and at galactic scales, is the NLR (Netzer 2013).

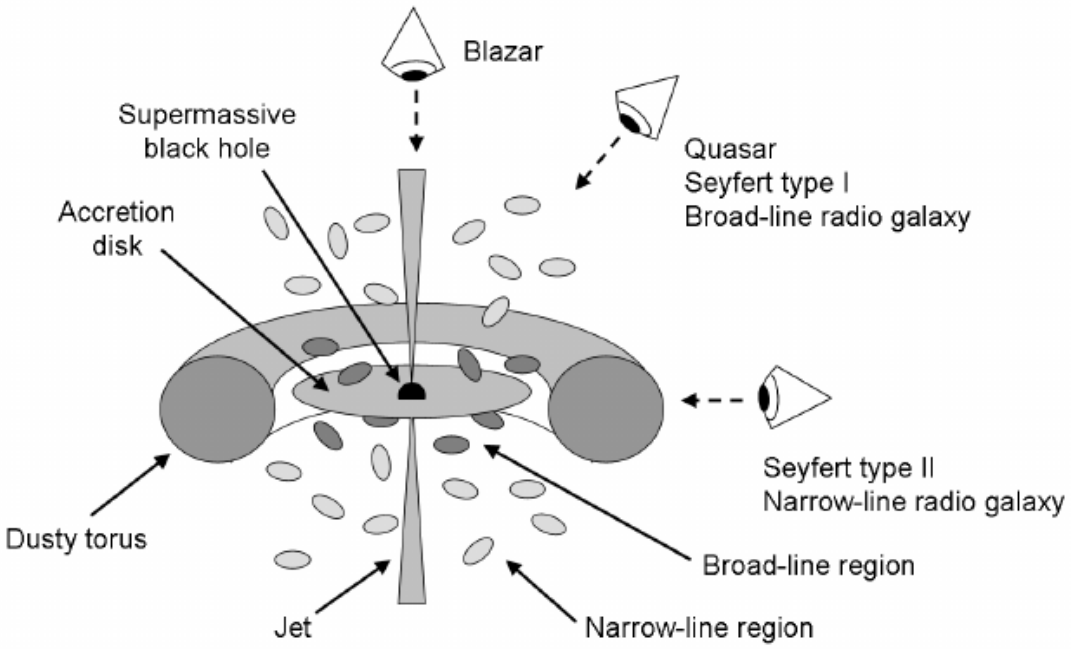

Figure 1.1: The orientation-based unification model showing the various different classifications for AGNs based on the angle at which the system is viewed by the observer. Figure taken from Zackrisson (2005).

The central engine power is generated through the process of accretion. As material falls towards the black hole, a spiralling structure called the accretion disc is formed. Material closer to the black hole will move at a faster rate than that further

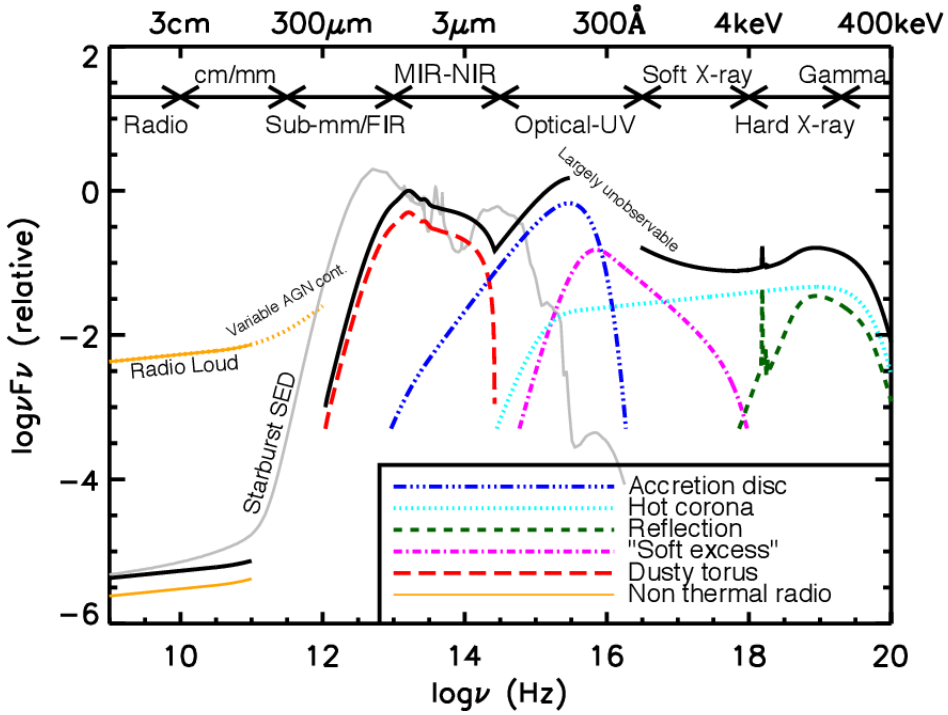

Figure 1.2: Spectral energy distribution (SED) for a typical AGN. This SED ranges from the radio band to the gamma band, and includes the contributions from various different components (as labelled). Figure taken from Harrison (2014).

away. These regions of material will interact with each other via some viscous process (Starling et al. 2004), which will convert gravitational potential energy into radiation and transfer angular momentum from the inner regions of the disc to the outer regions. This sustains the spiralling disc as the material continues to flow inwards (Gallo 2011). An important structure parameter for the accretion disc is λ, which is a parameter that characterizes the accretion rate, and is defined as:

$$\lambda = \frac{L_{bol}}{L_{Edd}} \tag{1.1}$$

where L_{bol} is the bolometric luminosity and L_{Edd} is the Eddington luminosity (maximum luminosity to maintain balance between the outward radiation pressure and the inward gravitational force on the ionized hydrogen gas). For values ranging from $\lambda = 0.01$ to $\lambda = 0.3$, the accretion disc can be treated as geometrically thin, optically thick, and radiative-efficient, and is known as a Shakura-Sunyaev disc (Shakura & Sunyaev 1973). The accretion disc radiates like a blackbody with a temperature of 10^4-10^5 K and is the main source of UV photons in AGN.

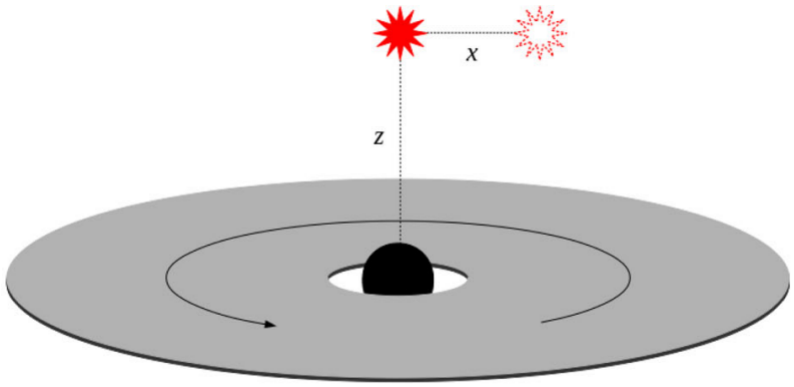

Figure 1.3: Shown here is a diagram of the lamppost model commonly used to represent the geometry of the AGN corona. This involves a cloud of hot electrons located at some height, z, above the black hole spin axis and displaced some distance, x, from said spin axis. Figure taken from Gonzalez et al. (2017).

The hot electron corona is a cloud of electrons that are moving at relativistic speeds. High thermal velocities of the electrons are brought on by the high temperatures of this electron cloud (up to 10^9 K). Its origin is not known for certain, however, it is believed to be similar to the origin of the solar corona. Magnetic fields in these regions are capable of dredging up material from the accretion disc over great distances

due to constant re-connection of magnetic field lines (Gallo 2011). The trajectories of charged particles, such as electrons, are affected by the surrounding magnetic fields, so line re-connection can launch many electrons out of the disc. Electrons are then deposited elsewhere in this central region, with the orientation generally being modelled by the aforementioned lamppost model. While the lamppost model is the most widely used assumption, alternate models have been proposed that might be more realistic. These theorized models include patchy, collimated (parallel rays of electrons), or extended clouds of electrons. Patchy coronae would have non-uniform electron densities (i.e., higher and lower density regions). Collimated coronae would consist of parallel rays of electrons (i.e., aligned like a beam). Extended coronae would be spread over a larger area and could have cylindrical, spherical, or conical geometries (e.g. Gonzalez et al. 2017). Depending on how frequently it interacts with other components, the corona is expected to be undergoing continuous changes on a variety of timescales.

Past the dust sublimation radius is an optically thick ring of neutral gas and dust called the dusty torus (Netzer 2013). The sublimation radius is the distance to the black hole at which temperatures are high enough for dust to evaporate and is given by:

$$r = 1.3 L_{UV,46}^{1/2} T_{1500}^{-2.8} \; pc \tag{1.2}$$

where $L_{UV,46}$ is the UV luminosity in 10^{46} ergs/s and T_{1500} is the temperature at which

dust grains evaporate, in units of 1500 K (Barvainis 1987). Since the inner torus is believed to be composed of graphite dust grains, this radius applies to the temperature at which graphite would evaporate. This dusty molecular structure is also formed at parsec scales (Hönig 2019). The torus is likely a very inhomogeneous structure (i.e., overall clumpy instead of smooth) and, much like with the corona, is likely not to be static in time. Accretion of material towards the SMBH means that the environment in AGN is quite dynamical, due to the presence of inflows and outflows (Hickox & Alexander 2018).

Two distinct regions known as the BLR and the NLR also exist in AGN. Their differences are manifested in the appearances of the emission lines seen from both regions. Not only is the BLR highly ionized by the central engine, but optical emission lines originating from the region are also seen to be broadened from Doppler broadening, as some material in the central region moves away and some moves towards the observer (i.e., redshifted and blueshifted, respectively) (Gallo 2011). On the other hand, emission lines from the NLR do not experience any significant Doppler broadening effects (Groves 2007). This is region is considered an AGN component due to it being photoionized by the central engine, but its motion is dictated by the smooth gravitational potential of the host galaxy.

Within some AGN is the ability to produce jets, something that is not present in normal galaxies. Jets are highly collimated outflows that emerge from regions close

to the SMBH, and could have a base coinciding with the hot corona. These jets expel highly ionized gas outwards at relativistic speeds. Interactions between the strong magnetic fields and the high spin of the SMBH are responsible for the production of such jets (Blandford et al. 2019).

The emission from these components create the spectral energy distribution (SED) of AGN, which is the energy emitted in every frequency (or wavelength) band (Figure 1.2 for a typical AGN). Disc emission is treated as radiating out like a blackbody (Tanaka et al. 2004), as shown with the dark blue line. Coronal emission takes the shape of a power-law cut off at some energy, as shown with the light blue line. The dusty torus is largely responsible for the so-called "IR bump" (Pier & Krolik 1992), shown with the red line, that appears in the infrared region of the SED.

1.1.2 The Unification Model

An extremely important consideration in how we view and classify AGN is the unification model (Figure 1.1). This model assumes every AGN is essentially the same, undergoing the same processes and having the same geometries. The only difference is the angle at which it is viewed through the torus. Thus, the viewing angle of the AGN determines which regions and processes we can actually examine. This results in the different classifications, such as Seyfert galaxies, radio galaxies (radio-loud and radio-quiet), and quasars/blazars. The latter classification involves the way in which

we view the jet in a jet-producing AGN. When the jet comes directly towards the observer, it is classified as a blazar. Otherwise, it is classified as a quasar.

Seyfert galaxies have high luminosity nuclei, however, they are intrinsically dimmer than quasars. Unlike quasars, host galaxy emission is still detectable in Seyferts. The Seyfert classification system goes from Seyfert I to Seyfert II, based on the angle at which the central engine is viewed. This results in us seeing different emission characteristics based on whether or not the dusty torus is obscuring the central engine along the line-of-sight.

Seyfert I galaxies are classified as galaxies where the central region is viewed directly. These types of galaxies have the advantage of not being obscured by the dusty torus. They provide a better view of the regions closest to the central SMBH. Spectra of Seyfert I galaxies show emission lines in the optical/UV spectra that are both very broad and strong. This owes to the fact that we have a better view of the BLR and central region, where such emission lines become more dynamically broadened.

Seyfert II galaxies are classified as galaxies at which the central region is heavily obscured by the dusty torus. This allows us to analyze the properties of the dusty torus in better detail. Emission lines in Seyfert II galaxies are not nearly as broad as those in Seyfert I galaxies, since we only see the NLR and not the BLR. In addition to these two classifications, there are various intermediate types, which are based on orientations between these two extremes.

Integrated within this unified model is a classification based on the strength of the AGN radio emission, where AGN will either be classified as radio-loud or radio-quiet. They are often classified based on their radio-loudness parameter:

$$R = \frac{L_\nu(5\text{ GHz})}{L_\nu(4400\text{ Å})} = 1.36 \times 10^5 \frac{L(5\text{ GHz})}{L(4400\text{ Å})} \tag{1.3}$$

where $L(5\text{ GHz})$ is the 5 GHz luminosity density (corresponding to radio band) and $L(4400\text{ Å})$ is the 4400 Å luminosity density (corresponding to the optical B-band) (Netzer 2013). This indicates how strong the radio emission is compared to the optical, with $R \geq 10$ corresponding to radio-loud AGN and $R < 10$ corresponding to radio-quiet AGN.

Radio-loud AGN are generally associated with early-type galaxies (e.g., ellipticals) (Wilson & Colbert 1995; Xu et al. 1999). The major source of the radio emission in these AGN is from relativistic jets. In this case, the emission is the result of synchrotron emission, where relativistic electrons moving through a magnetic field are accelerated perpendicularly to their motion (Panessa et al. 2019). These jets can power radio lobes, which are large-scale structures that are found to be located on both sides of the AGN. In these AGN, much of the bolometric luminosity goes into powering these jets (Wilson & Colbert 1995).

Radio-quiet AGN are mostly seen in late-type galaxies (e.g., spiral and S0 galaxies), and are the more common of the two classifications (Wilson & Colbert 1995; Xu

et al. 1999; Panessa et al. 2019). These AGN have weak radio emission and the ejecta from such AGN do not contribute significantly to the energetics of the galaxy (Wilson & Colbert 1995). Since such AGN lack the presence of a jet, which would otherwise be the dominant process we observe, these AGN allow for studying of the alternate sources of radio emission (Panessa et al. 2019).

1.1.3 X-ray Emitting Region

Spectra (plot of brightness versus energy) and light curves (plot of brightness versus time) of AGN provide useful information about the source and the environment in the central region. The presence of certain materials in these regions can be noticed by the emission lines, absorption lines, and edges seen in spectra.

Emission lines are formed when an electron transitions to a lower energy level in an atom. Conversely, absorption lines are narrow, sharp decreases in brightness that are the result of electron absorbing a photon. Absorption edges are sharp discontinuities that follow a decrease in brightness, and occur from the ionization of a ground-state electron where enough energy is absorbed to surpass the energy binding the electron to the atom. As there is now an opening to fill in the ground-state, another electron can de-excite to the ground state, which would result in an emission line alongside the absorption edge. To measure spectra, X-ray photons produced from AGN must first be detected. To do so, we make use of detectors on X-ray telescopes. These record

the time of photon arrival and the energy with which it is detected (see Section 1.4).

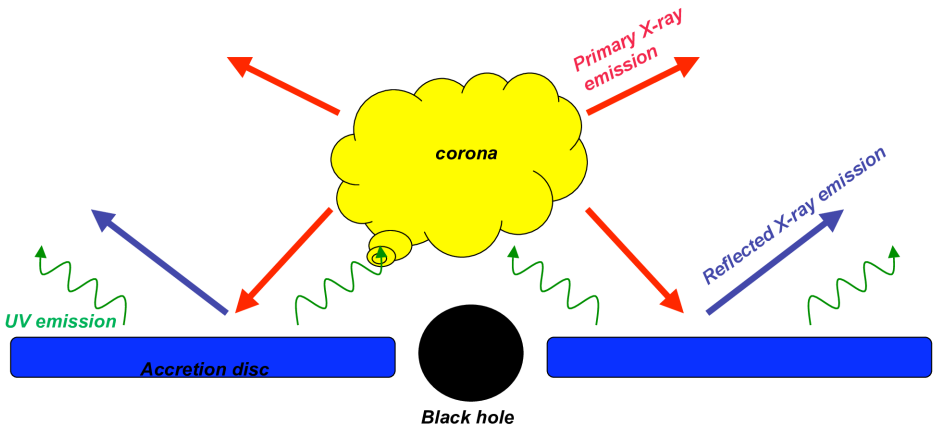

Figure 1.4: Simple sketch showing the interactions between the corona and accretion disc. Some UV emission from the disc is emitted towards the corona which, in turn, both emits some towards the observer and some back towards the disc, resulting in the reflected emission. Figure taken from Gallo (2011).

The primary source of the X-rays seen in AGN is the hot electron corona. The corona is configured in some unknown geometry around the black hole and inner disc. Some UV photons emitted from the accretion disc will traverse the corona (Figure 1.4). When this happens, the UV photons are Comptonised. In this process, disc UV photons collide with hot coronal electrons and are up-scatted to higher energies (i.e., X-rays). When photons interact with the corona in this way, they are emitted

isotropically. Thus, some of these photons are emitted towards the observer and detected as the primary emission component in the X-ray spectra of AGN (red curve in Figure 1.5). This component is featureless and, as mentioned previously, takes the form of a power-law cut-off at some high energy that depends on the coronal temperature.

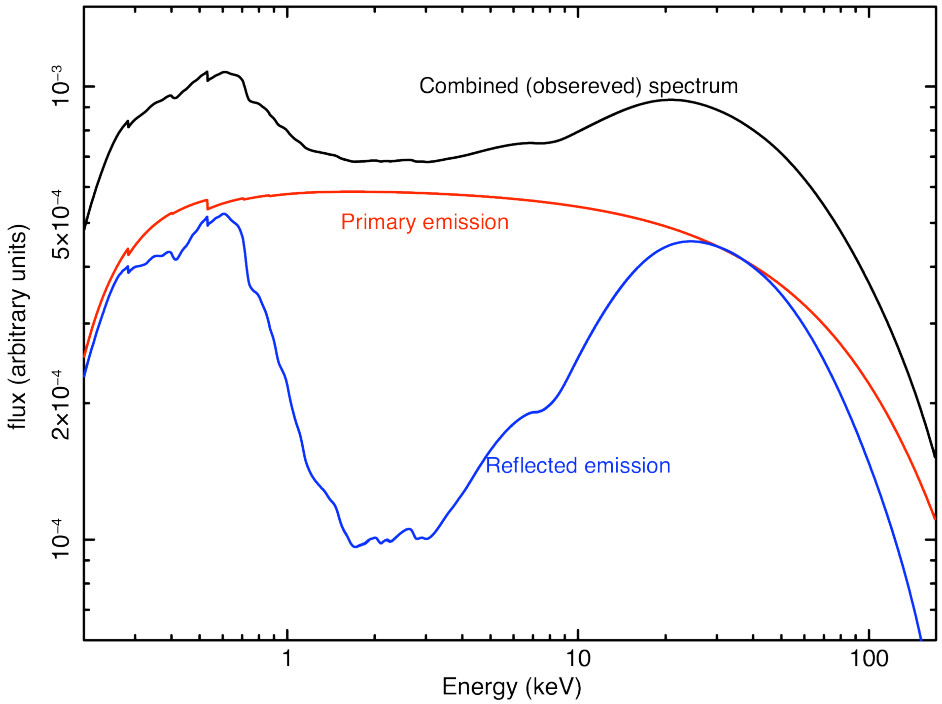

Figure 1.5: Plot showing the combined X-ray spectrum of a typical AGN that is the result of both the primary emission component from the corona (red) and the reflection component from the disc (blue). Figure taken from Gallo (2011).

Some of the isotropically emitted coronal emission will be directed back towards the accretion disc, resulting in the reflection component seen in AGN spectra (see

Figure 1.4). The disc, being much cooler and denser than the corona, can either absorb or scatter these incoming photons. Absorption of these photons is dependent on the energy of the photons, with lower energy photons (i.e., soft X-rays) tending to be absorbed and higher energy photons (i.e., hard X-rays) being scattered. The absorption of these photons can lead to fluorescence. In this process, the photons ionize heavier atoms (i.e., metals), causing photons to be emitted as the excited electrons in the atom relax to a lower energy level. Photons that are not absorbed, but have still interacted with the disc, are then Compton scattered by electrons in the disc. This results in the reflected emission component (blue curve) in Figure 1.5. Through fluorescence, a variety of atomic features are imprinted onto the spectrum, carrying details about the composition of the disc (Reynolds 1999). The most noticeable of these features is the Fe Kα emission line at an energy of $\sim$6.4 keV. Iron is quite prone to fluorescence and it is not surrounded by very many lines and, thus, it is less likely to be blended with other features.

The AGN environment can have a few large effects on the emission line profiles, such as for the Fe Kα emission line. The first of these effects, Doppler broadening, leads to a distinctly double-peaked profile. This happens because radiation from the central engine is both blueshifted and redshifted from the perspective of the observer, due to the rotation of the accretion disc. The second of these effects, special relativistic broadening, results in an asymmetric line profile. This effect happens when

material is moving at relativistic speeds in regions close to the SMBH. Beaming of light from matter moving toward the observer is responsible for this effect, making the blueshifted side of the disc much brighter. The third and final of these effects, general relativistic broadening, results in a stretching of the emission line profile to lower (redder) energies. In the closest regions to the SMBH, the gravitational influence of said SMBH is so strong that radiation gets "stuck" in a strong gravitational potential well. Escaping this well results in photons losing a significant amount of energy, which becomes higher the closer to the SMBH the photons come from. Figure 1.6 shows how each effect changes the appearance of emission lines.

Two other components often show up in X-ray spectra. As mentioned previously, the X-ray continuum emission for AGN is well-fit by a power-law, however, when extended below 2 keV it can reveal an excess of emission known as the soft excess, and when extended above 10 keV to about 80 keV it can reveal an excess of emission known as the Compton hump. These can both be seen in Figure 1.5.

The soft excess is a spectral component of particular interest, since its origin is still uncertain. To account for this excess, there are two main scenarios proposed: ionized relativistic blurring or thermal Comptonisation of disc photons by some optically thick and warm plasma. The former scenario would most likely require a high Eddington rate, and the level of relativistic blurring would be dependent on the inner radius of the accretion disc, since this most likely comes from reflection off of the inner accretion

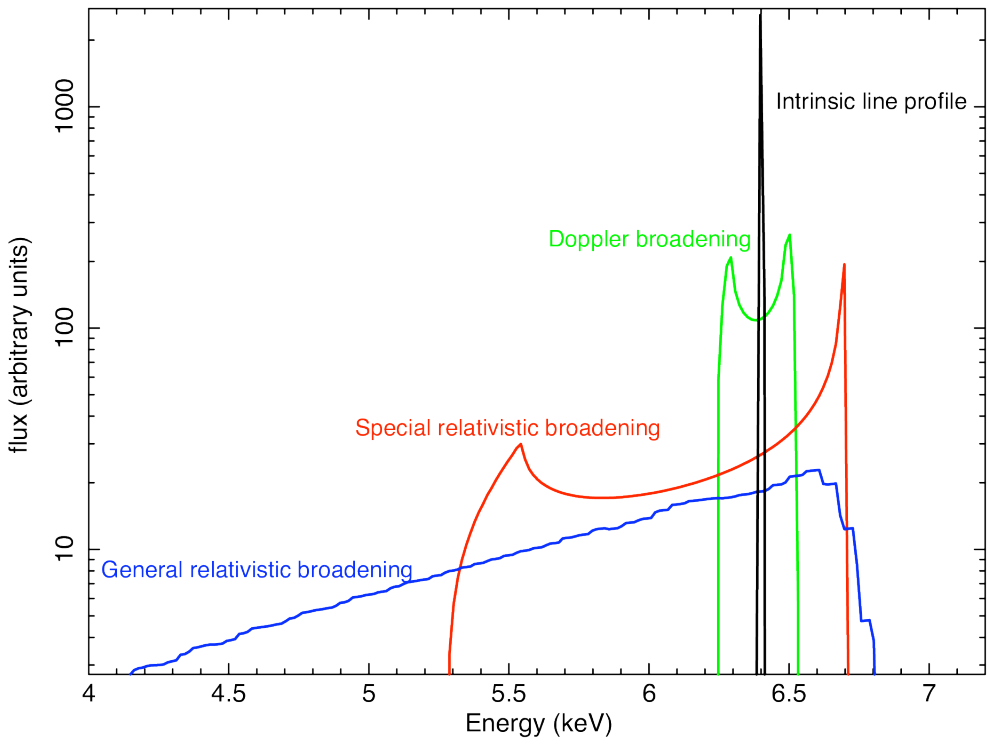

Figure 1.6: Shown here is how effects induced by the AGN environment can modify intrinsic line profiles (black). Doppler broadening (green) causes a double-peaked profile to appear. Special relativistic broadening (red) results in an asymmetric line profile. General relativistic broadening results in a stretch of the line profile to lower energies. Figure taken from Gallo (2011).

disc due to the proximity to the black hole. In this energy range, there are many emission lines near each other, so the broadening and blurring of the lines result in the huge hump that we see making up the soft excess (Fabian et al. 1989).

In the latter scenario, the soft excess originates from a second corona, generally referred to as a "warm" corona, that would likely have to be near the inner portions

of the accretion disc. Much like the hot corona, this warm corona would also involve scattering (through Comptonisation) of the seed disc photons, however, with less energy transferred to them than in the hot corona. Thus, it would result in lower energies (from UV to soft X-rays) of photons emitted from such a corona, explaining the lower energies of the soft excess (Petrucci et al. 2018).

The Compton hump component is analogous to the soft excess, although its origin is well-established. It is associated with the reflection component. In this range, photons are prone to a large amount of Compton down-scattering (Kara et al. 2015a; Kara et al. 2015b).

1.2 Absorption of the X-ray Region

The X-ray emission of AGN often experience absorption effects, particularly in the 0.1-10.0 keV range. In addition to absorption attributed to the Galaxy and the host galaxy along our line-of-sight (LOS), there are other forms of absorption that can occur in the AGN. The three main sources of absorption in AGN are by the dusty torus, obscuring clouds, and warm absorbers. The latter two can exist as outflowing winds in the AGN system.

Absorption from the dusty torus was briefly mentioned in the previous section, as the distinction between absorbed and unabsorbed AGN. Here, we go into more detail about the effects of torus obscuration on AGN X-ray emission. As mentioned,

absorption by the torus has a larger effect the closer to edge-on we view the system. Through absorption, the torus can reprocess high-energy photons to IR energies.

The torus is the protagonist in the unification model. To identify obscuration by the torus, there are various signatures we can look for. This component tends to "reflect" much of the power law continuum, something that is dependent on how much of the source is covered by the torus. Two main signs that point to reflection by the torus are a 30 keV reflection hump and the presence of the narrow Fe Kα line (Ricci et al. 2014). The torus likely contributes considerably to the flux of Fe K lines. It is expected that the torus should absorb a significant amount of the luminosity from the central engine, meaning it should exhibit its own emission. Heating of the torus via central engine optical/UV/X-ray photons results in thermal emission in the infrared (Pier & Krolik 1993).

Ionized or warm absorbers (WAs) are important sources of absorption in Seyfert 1 AGN. This type of absorption occurs as primary X-ray emission passes through slow-moving, highly-ionized winds along the LOS. In the past, studies have tried to unravel if WAs could be from accretion disc winds, but much evidence has pointed towards a scenario involving winds from the torus (Blustin et al. 2005; Laha et al. 2014; Laha et al. 2016). Either way, it is not fully known which is truly the case, but WAs tend to be found on scales closer to the torus (i.e., outer edges of BLR or far beyond the BLR) (Reynolds & Fabian 1995; Blustin et al. 2005).

Absorption lines associated with such absorbers tend to be from elements with atomic numbers around and including oxygen. Absorption K-edges such as O VII and O VIII are dominant features of warm absorbers in spectra, with some also showing edges from other metals, such as Ne IX and Ne X (Reynolds & Fabian 1995). Since spectra for warm absorbers show the absorption lines to be blue-shifted compared to the host-galaxy frame, the material must be outflowing. These types of outflows are very common, seen in approximately 50% of Seyfert 1 galaxies (Crenshaw et al. 1999). The ionization parameter, $\xi = L/nr^2$, measures the degree to which the absorber is ionised. Here, L is the source luminosity, n is the number density, and r is the distance from the source. WAs exhibit a large range of ionization parameter values and most AGN will contain WAs with multiple phases of ionization (Blustin et al. 2005; Laha et al. 2014).

WAs are likely to be clumpy (discrete distribution of absorbers) and have a low volume filling factor (Blustin et al. 2005; Laha et al. 2016). Since increases in the continuum flux have been seen to be linked to increases in the absorber ionization, this indicates that the central engine is responsible for photoionizing WAs (Krongold et al. 2007; Chakravorty et al. 2009). These types of absorbers are parameterized by their column densities and outflow velocities, and can often be partially covering the source (Krongold et al. 2007).

Winds in the AGN environment are very important for the movement of material

through these systems. Additionally, they are useful for transporting angular momentum from inner regions outwards (Murray et al. 1995). As already discussed, transfer of angular momentum throughout the disc is useful for a continual accretion flow inwards. AGN winds are either in the form of magneto-hydrodynamic (MHD) winds or radiative winds. MHD winds are launched along magnetic field lines, since magnetic fields in these regions can be strong enough to move material (Blandford & Payne 1982). Radiative winds occur when radiation pressure leads to high enough velocities for material to surpass the escape velocity for the disc. Interior to the launching radius, which is the radius at which the forces due to radiation pressure are higher than the gravitational forces within the disc, these winds will fail and fall back down to the disc. It is believed that these failed winds could make up the BLR (Giustini & Proga 2021). Successful winds are those launched beyond this radius.

Other than these two obscuration scenarios mentioned, there are still many alternate types of obscuration that can occur, which are generally classified as obscurers. These objects will tend to partially obscure the source as they pass along the LOS, and are located close to the AGN (i.e., in the BLR). The fraction of obscuration is given by the covering fraction parameter, f_c. Obscuration scenarios are constantly being studied in AGN and they can be the result of various things such as disc winds or gas clouds in the BLR. While these obscurers can experience changes in ionization state, they are more often seen to experience variations in covering fraction and

column density (the amount of material along the line-of-sight). These parameters are more directly related to the obscurer geometry. Thus, the variability seen due to absorption of AGN is often due to changes in the obscurer geometry (Tanaka et al. 2004). For example, if some non-uniform cloud is absorbing the AGN, as it passes along our LOS, different parts of the cloud will be covering the source and reveal more or less of the AGN light.

It is likely that many of these obscurers are patchy (i.e., have "holes" in them as they pass along the LOS). These are generally treated as a discrete distribution of many different clouds. These clouds are generally more likely to be ionized due to the close proximity to the BH, since photons from the corona do not have to travel as far to photoionize the material in the clouds. The material in these clouds can have different elemental compositions, which we can gain insight into through the analysis of AGN spectra.

These types of events can produce eclipses as they move across our LOS, analogous to those seen from exoplanets crossing in front of their star. Analyzing these light curves of these events gives us the opportunity to measure sizes in these regions, particularly of the source of the X-rays, making use of the fluctuations in the brightness of the source due to the obscurer. Since current telescopes cannot directly observe/resolve these regions due to their relatively small size scales (cosmologically-speaking), alternate methods for measuring sizes such as these are very useful.

1.3 Colour-Colour Analysis

Hardness ratio (HR, also an X-ray "colour") studies have seen wide use in studying of AGN, due to the many advantages that they provide. The most significant of these advantages is their applicability in situations where there are low photon counts. This is often the case when dealing with variability that occurs on short timescales, as current instruments do not offer enough signal-to-noise to build spectra in those situations, and robust spectral models become difficult to constrain. The HR is a ratio of count rates in different energy bands (HR = $\frac{H-S}{H+S}$), where H is hard (high energy) counts and S is soft (low energy) counts. Hardness ratios are less affected by low signal-to-noise and this results in HRs being useful in studying absorption, which has a larger effect at lower energies. Generally, dips in a light curve coincident with increases in an HR curve indicate an obscuration event (Brenneman et al. 2013).

Applications of HRs are useful in allowing for the studying of spectral shapes, and are often used alongside spectral analysis. HRs have particularly seen use in the identification of absorbed and unabsorbed sources in surveys (Schartel et al. 1996; Suchkov et al. 2006). There are some disadvantages that come with using HRs. Since HRs relate counts in different energy bands, they can be rather sensitive to chosen bands. This generally stems from the specific spectral components that are being probed when certain bands are used.

A newer take on this idea is the use of colour-colour (i.e. two different HRs) grids

to explore parameter variability within different models for a source. Changes in a model parameter can result in predictable changes on a colour-colour grid (i.e. a plot of colour versus colour). Such analyses involve overlaying data of interest onto such a grid, as these data would follow different tracks corresponding to different parameter variations. The general definition used for colours in this case is given by Equations 1.4 and 1.5, where S, M, and H are count rates in different energy bands.

$$C_1 = S/M \tag{1.4}$$

$$C_2 = M/H \tag{1.5}$$

The colour-colour analysis done in this work is motivated by three different analyses. Those are the studies done by Nowak et al. (2011), Carpano et al. (2005), and Grinberg et al. (2020). A substantial amount of work was added to the applications of colour-colour grids by Grinberg et al. (2020) (hereafter referred to as GR20), so they are the main motivation for this work.

The work of GR20 used such grids to study the high-mass X-ray binary (HMXB) known as Cyg X-1. It was framed as a way to overcome a central issue seen with spectral analysis in occassions when there are few photon counts. Having a lack of detail in these cases results in model degeneracies, where multiple different models

are seen to fit data equally well. However, the better resolution achieved with this method provides an opportunity to overcome this issue.

In their work, the grids were used to analyze the source of variability in this HMXB. HMXBs, which are binary systems consisting of a massive companion star and either a neutron star or black hole that accretes from this star, are often variable. This X-ray variability can be due to the absorption from clumps of material along the LOS. These clumps tend to originate from the stellar winds in these systems. The analysis done in this work focuses on this type of absorption variability. Models used include partial covering absorption, and different levels of ionization.

The data for Cyg X-1 in GR20 is from observations taken by the Chandra X-ray Observatory. As such, their colour-colour grids are constructed from Chandra HETGS/MEG responses. Since different telescopes are sensitive at different energies, the appearances of these grids will vary between them. Thus, the appropriate telescope response is accounted for.

They modelled the source with a partially absorbed power-law with different combinations of the varied parameters: photon index (Γ), column density (N_H), and covering fraction (f_c), at different ionization types (warm, neutral, etc.). Combining this with the response, they constructed colour-colour grids (one of these grids is shown in Figure 1.7). The observation of Cyg X-1 was subsequently compared to tracks from these grids.

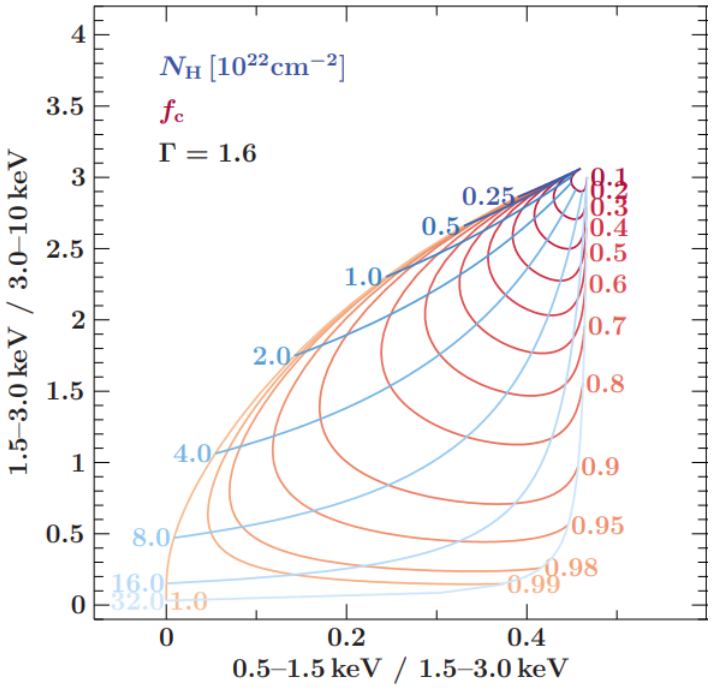

Figure 1.7: This shows an example of a colour-colour grid used in Grinberg et al. (2020). The energy bands used are 0.5-1.5 keV (S), 1.5-3.0 keV (M), and 3.0-10.0 keV (H), with the colours being calculated based on Equations 1.4 and 1.5. Photon index is constant at $\Gamma = 1.6$, while covering fraction (red) and column density (blue) are varied.

Through these comparisons, they learned numerous things. Colour-colour grids allowed them to pinpoint the source of variability. For Cyg X-1, it was connected to an ionized partially covering absorber, whose changes in covering fraction and ionization are likely responsible for the variability. Additionally, this best case showed an inverse dependency between ionization and column density. These conclusions showed that colour-colour grids can have success when studying X-ray variability for HMXBs. It is then reasonable to believe that these grids could also prove useful with AGN, another variable X-ray source. This success motivates my work with colour-colour grids.

Carpano et al. (2005) applied these grids to the dwarf galaxy NGC 300, to study its optical disc. The goal was to determine X-ray properties of various point sources within the disc, with the grids being used to help analyze the dimmer point sources. These point sources would not be sufficiently bright for spectral analysis to provide useful information. For their grids, they considered just a simple bremsstrahlung model, as well as a combination of a bremsstrahlung and a power law model. Grids were constructed with different combinations of the varied parameters: photon index, column density, and temperature of the disc. Through comparisons of these grids with a set of point sources, they were able to determine the appropriate models for all of the point sources, excluding one of them. Once again, we see a success in applying these grids within X-ray analyses.

Nowak et al. (2011) used these grids with Cyg X-1. Their work specifically looked at the galaxy's dust scattering halo, in an effort to inform of its optical depth. To do so, the general model consisted of an absorbed disc and power law. The grid was created with the optical depth being varied, and was subsequently compared to data from an observation of Cyg X-1 by Suzaku-XIS 1. There were problems with their grids, as they failed to fully represent the properties of the halo. However, they determined that it was more than likely due to relatively poor data quality. This work was followed up on by GR20, which as mentioned ended up being much more successful in the applications of colour-colour grids.

1.4 X-ray Telescopes

Data from two different X-ray observatories were used in this work. Here we provide a brief description of each.

1.4.1 XMM-Newton

The X-ray Multi-Mirror Newton Observatory (XMM-Newton) is a space-based observatory widely used in X-ray astronomy. The large effective area of its three X-ray telescopes and its ability to cover a wide range of energies makes XMM-Newton a workhorse in AGN studies. Its goal when it was launched on December 10th, 1999 was, in part, to generate better observations of faint sources (Jansen et al. 2001).

There are various instruments aboard XMM-Newton that offer different capabilities. There is the European Photon Imaging Camera (EPIC) that contains three CCD imaging cameras. There is a pn CCD and two MOS (Metal Oxide Semi-conductor) CCDs (Jansen et al. 2001). The pn CCD consists of 12 CCDs, each with dimensions of 3 cm by 1 cm, which leads to a high photon detection efficiency. For use in high resolution spectroscopy, there is the Reflection Grating Spectrometers (RGS) (den Herder et al. 2001). A Wolter 1 design is used for the telescope optics.

1.4.2 Swift XRT

The Swift Gamma-Ray Burst Mission was launched November 20th, 2004 with the aim to better understand gamma-ray bursts (GRBs). It carries three instruments: Burst Alert Telescope (BAT), X-ray Telescope (XRT), and Ultraviolet/Optical Telescope (UVOT). The latter two are of most importance to this work. The XRT is a narrow-field X-ray telescope, with an energy coverage of 0.2-10.0 keV. It makes use of a grazing incidence Wolter 1 telescope, and is able to make measurements over a wide range of fluxes (>7 orders of magnitude) (Gehrels et al. 2004).

The UVOT also covers a narrow field, but covers a wavelength range of 170-600 nm. This instrument can make observations in six filters: V (5050 Å-5800 Å), B (3900 Å-4900 Å), U (3050 Å-3900 Å), UVW1 (2250 Å-2950 Å), UVW2 (1650 Å-2250 Å), UVM2 (2000 Å-2500 Å).

An online tool is available that allows for the building of "products" for Swift observations. This tool, called the Swift Product Builder[1], allows for the building of spectra and light curves. These capabilities were taken advantage of for much of the data shown in this work. By specifying a source, whether through name, target IDs, or coordinates, it finds all available Swift observations for that object. There is the ability to choose all observations or to specify certain ones. To build spectra, it can be chosen whether it is one for all observations or specific ones (user-defined, per

[1] `https://www.swift.ac.uk/user_objects/`

snapshot, per ObsID). Light curve building allows for energy range specifications, and offers different binning options (time, counts, snapshot, or observation). Swift product building is also available on Python through the package SWIFTTOOLS. Products can be sent to the user's e-mail, downloaded from the site itself, or downloaded through Python (Evans et al. 2009).

1.5 This Work

In this work, spectral and timing techniques will be used to study transient behaviour in two AGN: NGC 6814 and Zw 229.015. For NGC 6814, we use colour-colour grids to study the X-ray variability occurring as a result of an obscuration event (Chapter 2). The main goal is to probe the geometry of the absorber responsible for the obscuration and to assess what other pieces of information we can gather about these events. By tracking these data in colour-colour space, the grids can inform us of the absorber variations occurring within the source (Chapter 3).

The work for the second source, Zw 229.015 (Chapter 2), started from interest in studying a transient, eclipse-like event, in a different source. Built off the work from Tripathi et al. (2019), this study goes into further detail on the transient event. We use spectral fitting to understand the mechanism for the variability. Scenarios tested include various types of absorption (including a partially covering obscurer) and intrinsic AGN variations (Chapter 4).

The layout of this thesis is as follows. Section 2 provides some important background on the two sources in this research. Section 3 contains the colour-colour analysis of NGC 6814, which has been published as Pottie et al. (2023). Section 4 outlines all of my work on Zw 229.015. Section 5 compares the results for these two AGN, and makes concluding remarks about both.

Chapter 2

Background on the Sources

2.1 NGC 6814

The first of the two AGNs studied is NGC 6814. NGC 6814 is a Seyfert 1.5 galaxy at $z = 0.00521$, that is seen to experience much X-ray variability over various timescales. Of most importance, it was witnessed to experience an eclipsing event in 2016. This eclipse was attributed to some absorber in the system, whose geometry has been studied in some detail (Gallo et al. 2021).

The eclipse in 2016 was captured almost entirely in one observation, which is quite rare. The eclipse happened on day-long timescales, which would indicate it being rather close to the SMBH. Analysis in Gallo et al. (2021) determined the mass

of the SMBH ($M_{BH} = 1.09 \times 10^7\ M_\odot$), the location of the obscurer ($r = 2694\ r_g = 4.34 \times 10^{15}$ cm; $r_g = \frac{GM_{BH}}{c^2}$), and the size of the X-ray source ($D_X = 26^{+3}_{-8}\ r_g = 4.20^{+0.54}_{-1.37} \times 10^{13}$ cm). Initial analysis on the eclipsing event, which draw similarities to exoplanet light curves, indicated a single homogeneous cloud to be a good match for the obscurer. This proposed geometry can be seen in Figure 2.1.

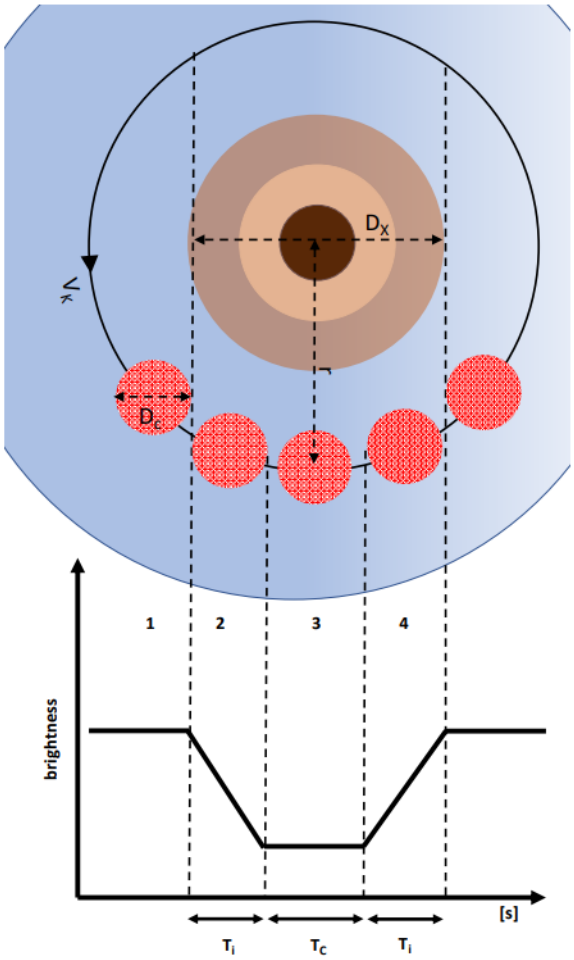

Figure 2.1: Proposed geometry for obscuration scenario in NGC 6814 based on the observed transient eclipsing event. Taken from Gallo et al. (2021).

Spectra of NGC 6814 show a weak to almost non-existent soft excess component.

Modelling of the spectra led to a rather complex model consisting of a cut-off power law and blurred reflector to model the X-ray source, while including modification by a partially covering obscurer and two warm absorbers (Gallo et al. 2021). In addition to this eclipse, it has been suggested that NGC 6814 might experience other occasional eclipses (Leighly et al. 1994).

2.2 Zw 229.015

The second AGN studied is Zw 229.015. It is a Seyfert I galaxy at $z = 0.0279$, in a host galaxy classified as a barred spiral (SBa). Reverberation mapping has determined a mass of $M_{BH} = 10^{6.94^{+0.14}_{-0.14}} M_{\odot}$ for Zw 229.015 (Williams et al. 2018). This source has been the subject of a fair amount of studies, but there is still much to be revealed about it. In 2011, it was seen to undergo a dip in both the X-ray and UV light curves. Studies such as Tripathi et al. (2019) have analyzed this dip. The source encounters relatively little absorption from the galaxy, with an absorption column density of $N_H \approx 6.25 \times 10^{20}$ cm^{-2} (Adegoke et al. 2017).

Many previous observations have been analyzed to examine the optical variability of the source. Between 2009 and 2018, there have been observations by Swift, XMM-Newton, Suzaku, NuSTAR, Kepler, and some ground-based telescopes. These observations have shown that the AGN exhibits variability on long timescales, but less so on short (hourly) timescales.

Kepler observations of this AGN have captured a remarkable amount of data, as it has been one of the brightest and longest observed AGN in the Kepler field. They have revealed an optical variability timescale of roughly 5 days (Edelson et al. 2014). The source experiences large optical variability on various timescales (Carini & Ryle 2012). A reverberation mapping study using the ground-based Lick 3 m telescope, and its Kast Spectrograph (and V-band imaging with Lick Observatory and Brigham Young University West Mountain Observatory) was carried out by Barth et al. (2011). Outside of obtaining a virial estimate of the source mass, they also noticed a more than doubling of the broad Hβ flux.

XMM-Newton observations have also been analyzed to some level, in studies such as Adegoke et al. (2017). In their work, the observations show the presence of a soft excess (below $\sim$ 1 keV) after fitting the data with a simple power law. They also find comparable fits between models for the relativistically blurred reflection (Section 1.1.3) and thermal Comptonisation (Section 1.1.3) scenarios, and can not distinguish the origin of the soft excess. Noticing a time lag of $\sim$ 1000 s between soft and hard bands pointed in favour of the thermal Comptonisation scenario, which leads to an estimate for the distance between the SMBH and the emission region of $\sim$ 20 R_g (Adegoke et al. (2017)).

Further analysis from simultaneous observations with XMM-Newton and NuSTAR was carried out by Tripathi et al. (2019). This includes further details on the X-ray

and optical/UV properties of the source. They note the Compton hump is negligible along with a lack of distinct features in the spectra. Further notes are also made on the variability of the source, based on the observations from the different telescopes. Tripathi et al. (2019) claim that the multi-epoch data point towards intrinsic changes due to variability of the power law component. Additionally, it is pointed out that other components like the disc or potential absorbers contribute little to the variability of Zw 229.015. This is said to suggest a large distance between the corona and the disc.

Chapter 3

Probing the Eclipse in NGC 6814 Using Colour Colour Grids[1]

The emission from Active Galactic Nuclei (AGN) is dominated by processes that occur in the regions closest to the central supermassive black hole. AGN have the capability to emit over the entire electromagnetic spectrum, but X-rays originate in the inner-most regions and their emission is highly variable. The processes creating X-rays largely occur from interactions between the hot central corona and the inner accretion disc. There are constituents within the AGN systems, e.g. the warm absorbers, obscurers, and the dusty torus, that give rise to absorption and modify the X-ray emission we see. Studying the absorption can yield valuable information about the

[1]Chapter 3 has been published as Pottie et al., 2023, MNRAS, 525, 3633. It appears as is in its entirety.

AGN environment and the region where the absorption originates from (Gallo et al. 2004; Chainakun & Young 2017; Alston et al. 2020; Miller et al. 2010). In the event of eclipses, we can even estimate sizes of the X-ray source, which is important since this region is not resolvable with current telescopes (Risaliti et al. 2007; Risaliti et al. 2009b; Risaliti et al. 2011; Turner et al. 2018; Zoghbi et al. 2019).

Significant X-ray variability in AGN can be attributed to the absorbers within the system, rather than intrinsic to the continuum source. Many AGN like NGC 1365, 3327, and 3783, have shown eclipses by some obscurer(s) (Risaliti et al. 2007; Risaliti et al. 2009a; Walton et al. 2013; Brenneman et al. 2013; Turner et al. 2018; George et al. 1998; De Marco et al. 2020; Costanzo et al. 2022). Often times, such an obscurer partially covers the source (Holt et al. 1980; Tanaka et al. 2004; Gallo et al. 2015; Kara et al. 2021), with the fraction denoted by the covering fraction parameter. Variability in these obscurers generally involves changes in the column density and/or the covering fraction of the obscurer as it transits the line-of-sight to the X-ray source, but variations in the ionising state can also occur. Brightness fluctuations because of the obscurer can be particularly useful at understanding the geometry of such clouds.

Eclipsing events are most evident when comparing the light curve and hardness ratio (HR) curve, simultaneously. Dips in light curve coincident with hardening in the HR curve generally signify an obscuration event (Brenneman et al. 2013). This happens because the absorption has a larger effect at softer energies. The variability

can occur on all timescales from hours (e.g. NGC 6814, Gallo et al. 2021; NGC 4395, Nardini & Risaliti 2011) up to years (e.g. NGC 5548, Kaastra et al. 2014) giving information about the location of the absorption (e.g. Bianchi et al. 2009).

Hardness ratios (colours) are regularly employed in X-ray astronomy to study spectral shapes. Colours are particularly useful in situations where photon detections are very limited and spectral analysis is challenging. They were widely applied to low-count data in the ROSAT All Sky Survey (RASS, Schartel et al. 1996), to classify objects (e.g. as absorbed or unabsorbed) and to measure photon indices.

The motivation to use colour-colour grids to study in this work comes from Grinberg et al. (2020). They used colour-colour grids to distinguish different models of high mass X-ray binaries (HMXBs). Applying these grids to Cyg X-1, they could understand the influence of different parameters and break the degeneracy between different models. The colour analysis could be used to discern the effects of changing covering fraction, column density, photon index, and different ionization types (neutral, warm, etc.) in partial coverers.

Similarly, colour-colour grids were used in the work of Carpano et al. (2005) and Nowak et al. (2011). The former applied such grids to point sources in the optical disc of NGC 300, allowing them to determine the model that described all but one of the point sources. The latter applied grids to the dust-scattering halo of Cyg X-1, and found success in discerning some properties of the X-ray source. Building on the

success of these mentioned works and others, here we adopt colour-colour grids to study the eclipse in NGC 6814.

NGC 6814, is a Seyfert 1.5 AGN ($z = 0.00521$) with a black hole mass of $M_{BH} = 10^{7.038^{+0.056}_{-0.058}}$ $M_\odot$ (Bentz & Katz 2015). It possesses strong X-ray variability on all timescales and it might exhibit occasional eclipses (e.g. Gallo et al. 2021; Leighly et al. 1994). The 2016 eclipse, was captured by *XMM-Newton* in its entirety (Gallo et al. 2021). In a continuous observation, the ingress, low-state, and egress were observed without interruption. Capturing an entire eclipse in an observation is rather unique, and it allowed for the determination of the size, shape and the location of the obscurer causing the eclipse (Gallo et al. 2021). The eclipse was observed to happen on day-long timescales, something that is consistent with an obscurer located sufficiently close to the black hole (e.g. the broadline region, BLR) (Elvis et al. 2004; Risaliti et al. 2009b; Puccetti et al. 2007; Bianchi et al. 2009; Svoboda et al. 2015). This is supported by the spectral and timing analyses of Gallo et al. (2021), where they also conclude that the data were consistent with obscuration from a single, homogeneous cloud.

In this work, we will apply a colour-colour analysis to the data from the 2016 eclipse in NGC 6814. Such grids will allow us to examine the eclipse with better time resolution than the "state-resolved" spectral analysis of Gallo et al. (2021). The generation of light curves is presented in Section 3.1. In Section 3.2, we describe the creation of the colour-colour grids. In Section 3.3, we explore different geometries of

the absorber(s) that might explain the colour-colour analysis. Results and conclusion of this analysis are then discussed in Section 3.4 and 3.5, respectively.

3.1 Data Processing and light curves

We use archival data obtained from the *XMM-Newton* (Jansen et al. 2001) Science Archive (XSA) for a long observation of NGC 6814 taken on 8 April 2016. Here we focus on the data collected by the EPIC pn (Strüder et al. 2001) detector, which were presented by Gallo et al. (2021), following their data reduction steps to extract calibrated event lists from the *XMM-Newton* Observation Data Files (ODFs) using the *XMM-Newton* Science Analysis System (SAS) version 20.0.0. Using the EPICLCCORR task, we produced light curves in four broad band passes: $0.3-10$ keV, $0.3-1$ keV, $1-4$ keV, and $4-10$ keV. Each light curve was rebinned into 1 ks time bins, and subsequently smoothed using a 5-point (i.e. 5 ks window) moving average to extract a cleaner representation of the underlying variable trend. In the forthcoming analysis, we ignore the final ~ 15 ks of the observation due to significant background flaring. We note that we only present the results for the smoothed light curves here, though our results and interpretation do not change when using the unaltered data.

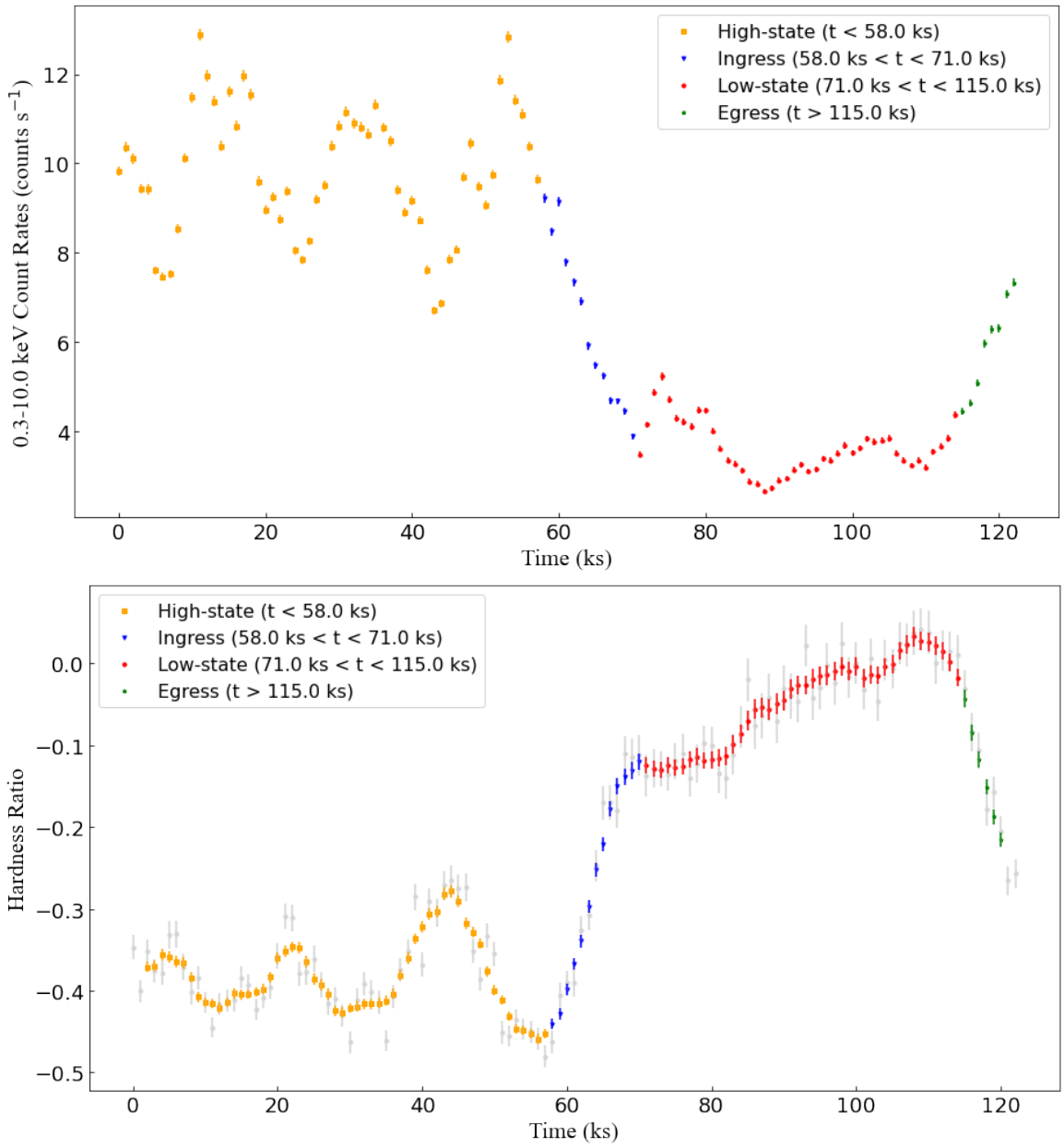

Figure 3.1: **Top Panel:** Light curve from the 2016 observation of NGC 6814 using the *XMM-Newton EPIC-pn* detector, with counts in the $0.3-10.0$ keV energy band. The uncertainties on the count rates are at the 1σ statistical level. **Bottom Panel:** Full HR curve (light gray) over-plotted with the smoothed HR, done by using moving average smoothing. For HR, the bands used are S $(0.3-1.0$ keV) and H $(4.0-10.0$ keV), with $HR = (H-S)/(H+S)$. The uncertainties on the HR are the 1σ count rate errors propagated through the moving average smoothing.

3.2 Colour-Colour Grids

Colours can be used to study AGN variability by examining the effects of different model parameters (or parameter combinations) in colour-colour diagrams. Comparing how a parameter is expected to change to how the measured colour changes can reveal what is driving the variability (e.g. Carpano et al. 2005; Grinberg et al. 2020; Nowak et al. 2011). In addition, colour changes can be measured with few photons so it is possible to examine variability and distinguish model degeneracies on much shorter time scales than with spectral modelling.

The count rates in each energy band depend on the telescope and instrument used, so colours are instrument dependent. To determine the predicted colours, a model of interest is chosen and folded through the appropriate instrumental response files. In this work, the *XMM-Newton*-pn responses generated in Section 3.1 are adopted.

The model adopted here is based on the best-fit partial-covering model in Gallo et al. (2021) that describes the eclipsing event in NGC 6814. The X-ray source was modeled as a power law (CUTOFFPL) and blurred reflector (RELXILLD), which was then modified by a variable partial coverer (ZXIPCF). All this emission was subject to two warm absorbers (XABSGRID) (Parker et al. 2019; Steenbrugge et al. 2003) presumably originating at large distances. In addition, a narrow Gaussian profile was included to model the narrow Fe Kα emission line at $\sim$ 6.4 keV. In XSPEC (Arnaud 1996) jargon, the model appears as: XABSGRID*XABSGRID * (ZGAUSS + ZXIPCF

Table 3.1: The best-fit continuum model adopted from (Gallo et al. 2021) and the variable partial covering parameters used for creating the colour-colour grid (Fig. 3.2). In XSPEC terminology, the best-fit model takes the form: XABSGRID*XABSGRID * (ZGAUSS + ZXIPCF (CUTOFFPL + RELXILLD))

Model Component	Model Parameter	Parameter Value
XABS_1	$\log\xi$/erg cm^{-2} s^{-1}	2.81
	$N_H/10^{21}$ cm^{-2}	25.0
	v_{out}/km s^{-1}	76.0
XABS_2	$\log\xi$/erg cm^{-2} s^{-1}	0.999
	$N_H/10^{21}$ cm^{-2}	3.59
	v_{out}/km s^{-1}	50.0
ZGAUSS	E/keV	6.45
	σ/eV	137
	Norm/10^{-5} ph. cm^{-2} s^{-1}	5.41
ZXIPCF	$\log N_H$/cm^{-2}	18 values: [21, 24]
	$\log\xi$/erg cm^{-2} s^{-1}	1.09
	f_c	0.56, and 9 values: [0.0, 0.8]
CUTOFFPL	Γ	1.99
RELXILLD	q_{in}	8.48
	q_{out}	3
	R_b/r_g	6
	a/[cJ/GM^2]	0.998
	i/$^\circ$	67
	$\log\xi$/erg cm^{-2} s^{-1}	0.326
	log N_H/ cm^{-2}	19
	A_{Fe}	3.39

(CUTOFFPL + RELXILLD)). Gallo et al. (2021) demonstrated that using a different continuum model did not significantly change the partial covering behaviour.

In Fig. 3.1, we see clear evidence of an eclipse. The top panel shows the light curve in the $0.3-10.0$ keV energy band, with the transient behaviour starting around 60 ks, where the brightness appears to exhibit the ingress, minimum, and egress stages of an eclipse. The HR curve alongside it (bottom panel) points to absorption as the source

of the variability. Concurrent with the decrease in count rate, there is a noticeable increase in HR ("hardening"), which is a signature of absorption.

The important component in this work is the variable partial covering absorber, since changes in its covering fraction (f_c, fraction of the X-ray source that is covered by the cloud) and column density (N_H) were sufficient to replicate the eclipse in NGC 6814. We vary these two parameters in our base model and extract the count rates in three specific energy bands to create the two colours used in the colour-colour diagram. Specifically, the two colours are:

$$C1 = S/M \tag{3.1}$$

and

$$C2 = M/H, \tag{3.2}$$

where $S = 0.3 - 1.0$ keV, $M = 1.0 - 4.0$ keV, and $H = 4.0 - 10.0$ keV. By varying through different combinations of covering fraction and column density, we create a grid in colour-colour space depicted by curves of constant covering fraction (red curves) and constant column density (blue curves) (Fig. 3.2).

In Fig. 3.2, the data from NGC 6814 and the partial-covering grid are over-plotted in colour-colour space. The colour combination shows a clear transition through four different states of the eclipse (e.g. high-state, ingress, low-state and egress). An

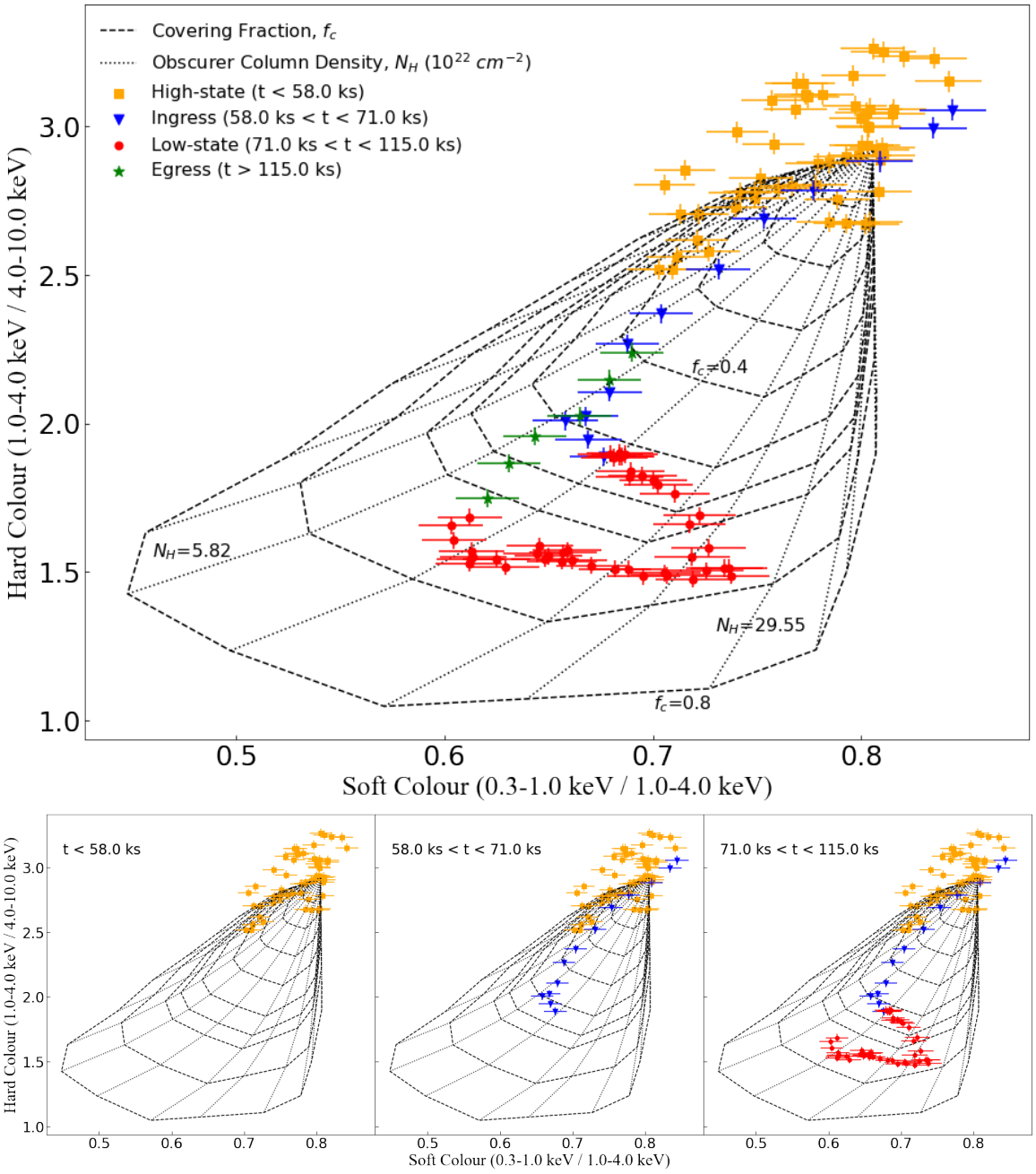

Figure 3.2: Colour-colour grid constructed from varying covering fraction and column density, plotted with data from NGC 6814. Curves of constant column density and constant covering fraction are shown in dotted and dashed lines, respectively. **Top Panel:** The complete figure with all the data plotted. The data are shown sequentially in the lower panels. **Lower-left Panel:** The high-flux pre-flare data. **Lower-mid Panel:** High-flux and ingress. **Lower-right Panel:** High-flux through to the end of the eclipse maximum. The egress is shown in the top panel. An animation portraying the evolution of the colours through time is available in the online version of the journal (Pottie et al. 2023). The uncertainties on the colours are the 1σ count rate errors propagated through the moving average smoothing.

animation portraying the time progression of the colours is available in the online version of the journal (Pottie et al. 2023).

The light curve and hardness ratio curve of NGC 6814 exhibit substantial fluctuations during the high-state prior to the eclipse ($t \leq 58$ ks) (Fig. 3.1). In Fig. 3.2, there is significant scatter in colour-colour space during the high-state (yellow data). This intrinsic variability is interesting and the subject of current work in preparation. Regarding the eclipse analysis, the intrinsic variations are not incorporated in the grids. Attempts to do so did not provide improvements over considering the obscuration alone. The changes after 60 ks are dominated by the eclipse. This could be because the high-flux variations appear to be driven by changes in the soft band, which are completely obscured during the eclipse.

During ingress ($t \approx 58 - 71$ ks), the changes in Fig. 3.2 (cyan data points), are dominated by changes in covering fraction, with only a slight shift in column density. With increasing time, the data points follow a curve of roughly constant column density ($N_H \sim 5.82$) while the covering fraction changes from 0 to ~ 0.8. The pattern is almost exactly reversed during egress ($t \geq 115$ ks) as the data move along the same track in the opposite direction, i.e. decreasing covering fraction with approximately constant column density.

The low state (red data, $t \approx 71 - 115$ ks) shows when the X-ray source is most highly eclipsed / obscured. In the light curve (Fig. 3.1), the count rate during this

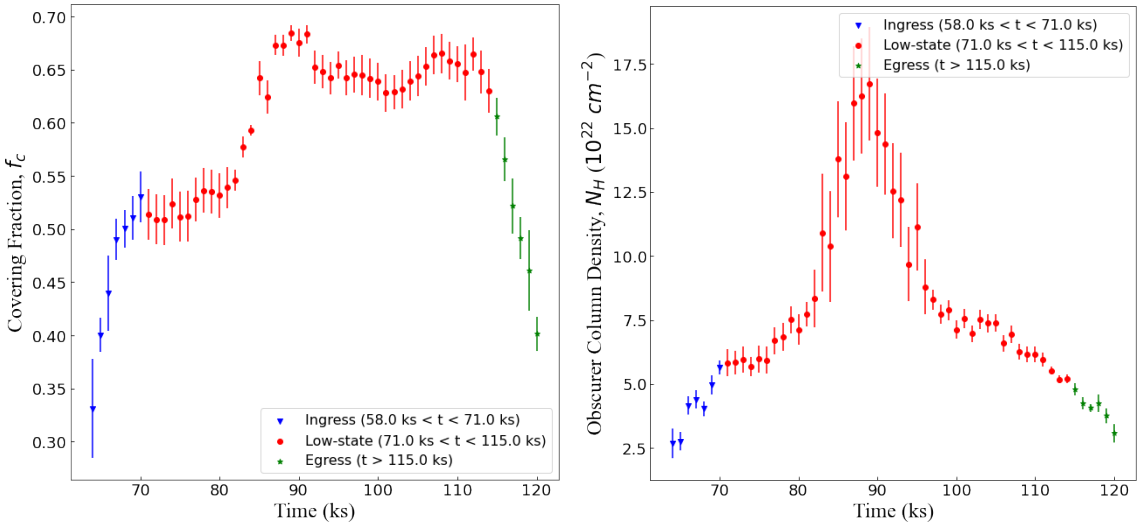

Figure 3.3: The changes in the covering fraction (**left**) and column density (**right**) as a function of time for the eclipse in NGC 6814. The curves cover the eclipse period between $60 - 120$ ks and the colours match the stages defined in Fig. 3.1 and 3.2.

phase is roughly constant. However, the hardness ratio curve (bottom panel, Fig. 3.1) displays a steady hardening during the low state even though the count rate is not varying significantly.

The colour-colour diagram (Fig. 3.2) can be used to explain this behaviour. While in ingress, the changes were dominated by the covering fraction increasing, during the first part of the low-state, the column density also begins to increase. At approximately 90 ks, the covering fraction and column density are both at their maximum values. This also corresponds to the lowest flux in the light curve (Fig. 3.1). After this point, while still in the low-state of the eclipse, the covering fraction remains constant while the column density begins to decrease.

The covering fraction and column density changes with time are presented in

Fig. 3.3. In the left panel, the covering fraction curve shows the expected steady increase and decrease during ingress and egress, respectively. There is a brief flattening in covering fraction evident at the start of the low state followed by a sharp rise at ~ 85 ks to a peak value. This is followed by a slight drop and further flattening until the end of the low-state (perhaps another peak at ~ 110 ks).

The right panel of Fig. 3.3 depicts the column density curve with time. From the start of ingress, there is a continuous, though not consistent rise to a maximum column density during the low-state. Similarly, from maximum column density there is a continuous, though not consistent drop to egress. In addition, the peak in column density does not occur at the mid-point of the eclipse. Understanding the variations in the covering fraction and column density of the obscurer during the low state is particularly important as it might reveal the nature of the medium.

To extract the column density and covering fraction for each data point, we employ the use of the SHAPELY package in PYTHON. Since most points on the grid are contained between two curves of constant covering fraction and two curves of constant column density, their positions on the grid can give approximate values for those two parameters. We interpolate between these curves of constant column density and covering fraction to obtain an (N_H, f_C) pair of values for each point on the grid. To determine the uncertainties on the interpolated values, the same processes is followed taking into consideration the relative uncertainty on the colour. Effectively, the 1σ

uncertainties on the colours are translated to uncertainties on the (N_H, f_C) pair.

The complexity in the shapes of both curves shown in Fig. 3.3 indicate the eclipse was not from the passing of a single, homogeneous cloud (Fig. 3.4). Fig. 3.4 presents the covering fraction and column density change predicted from simulations of single, homogeneous cloud passing in front of the X-ray source. For the simulation, the cloud is assumed to have a minimum column density and covering fraction at the beginning of the eclipse, reach a maximum in those parameters at the middle of the eclipse (i.e., the lowest flux/most absorbed state), and return to the minimum values at the end of the eclipse. The figure shows a uniform triangular shape for both curves clearly consistent with a simple increase to decrease scenario as would happen with such a cloud. This preliminary simulation, thus, shows that an alternate geometry is required to explain the eclipse, as will be discussed later in this paper.

3.3 Using More Realistic Modelling of the Obscurer

In addition to the single cloud obscurer, we considered three other scenarios to attempt to describe the behaviour in Fig. 3.3. Specifically, we looked at a double cloud model, a triple cloud model, and finally three clouds embedded in a highly ionized halo.

The objective is not to perfectly reproduce the covering fraction and column density changes seen in NGC 6814 (Fig. 3.3), but rather to determine if such contrived obscurers could create some of the behaviour seen in Fig. 3.3, like the flattening in

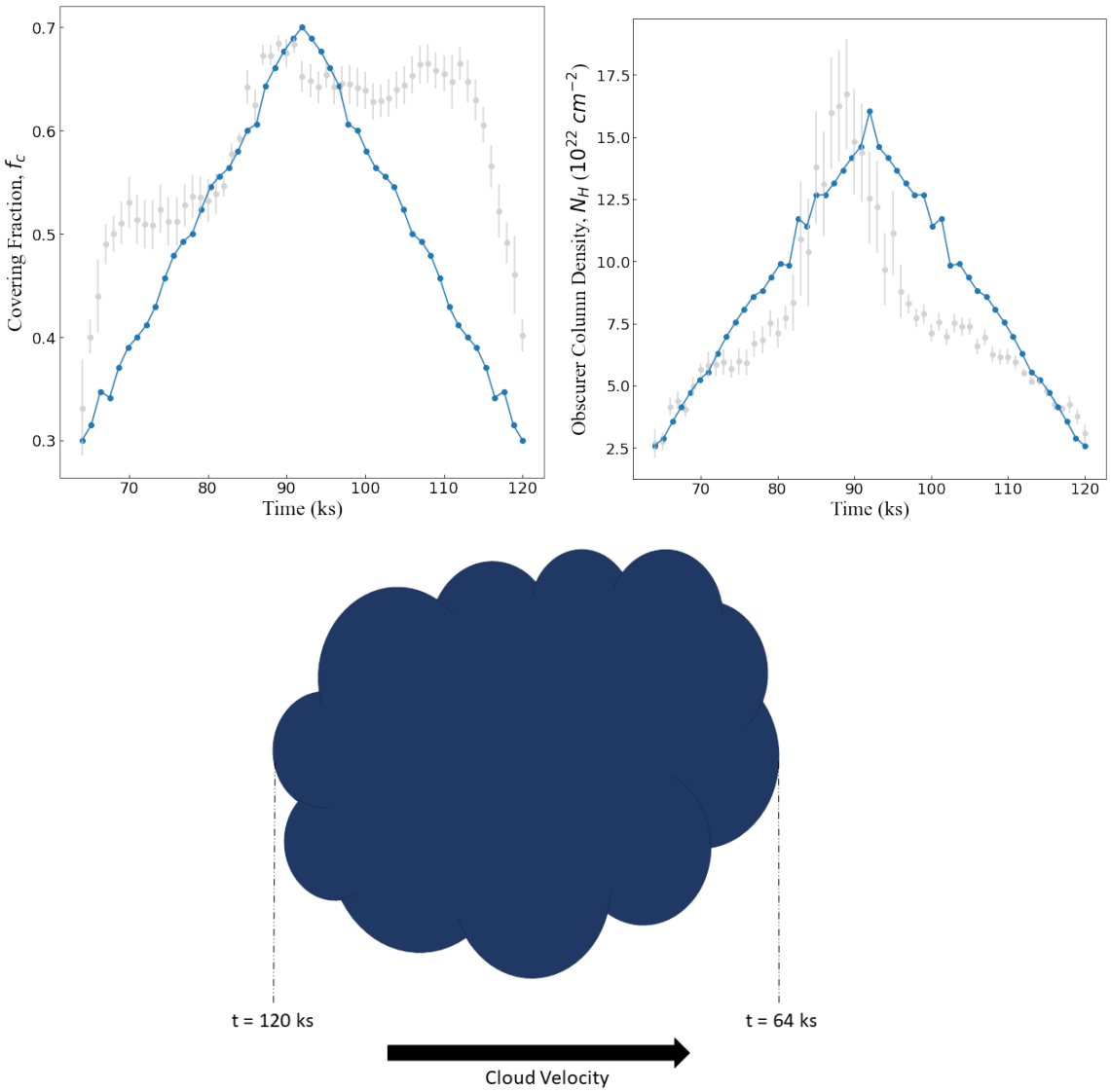

Figure 3.4: Simulation consisting of a single, homogeneous cloud showing the expected changes in covering fraction (**top left**) and column density (**top right**) as a function of time. A rough sketch of the single cloud system is also presented (**bottom**), showing how it would appear while crossing our line-of-sight (direction denoted by the cloud velocity). Dashed lines indicate start and end times. The simulated cloud varies in f_c from 0.3 to 0.7 back to 0.3, and varies in N_H from 2.5 to 15.0 back to 2.5, in units of 10^{22} cm^{-2}.

the covering fraction curve or the asymmetric peak in the column density curve.

3.3.1 Double cloud

In simulating the double cloud scenario, we consider a system consisting of two homogeneous clouds that partially overlap. Each cloud is modeled with a ZXIPCF component that has a variable covering fraction and column density. The ionization parameter ($\xi = L/nr^2$ [erg cm s^{-1}], with L being the ionizing luminosity of the source, and n being the cloud density a distance r from the source) of each cloud is fixed at $log(\xi) = 1.08733$. The degree to which the clouds overlap is arbitrary. In the simulation shown in Fig. 3.5, the clouds overlap for 30.625 ks.

The inclusion of a second cloud results in two peaks in the covering fraction curve corresponding to the times when each cloud covers the most. In between the peaks, the covering fraction curve flattens (Fig. 3.5, left panel). The multiple cloud scenario also introduces asymmetry in the column density curve (Fig. 3.5, right panel) where the peak column density is reached when the path-length through both clouds is maximum.

The exact location of the peaks and the duration of the flattening is dependent on the placement of the two clouds in the simulation. A larger separation would result in more distinct peaks. However, the flattening and asymmetry does resemble the behaviour seen in the original eclipse data (Fig. 3.3). These simulations are not exact

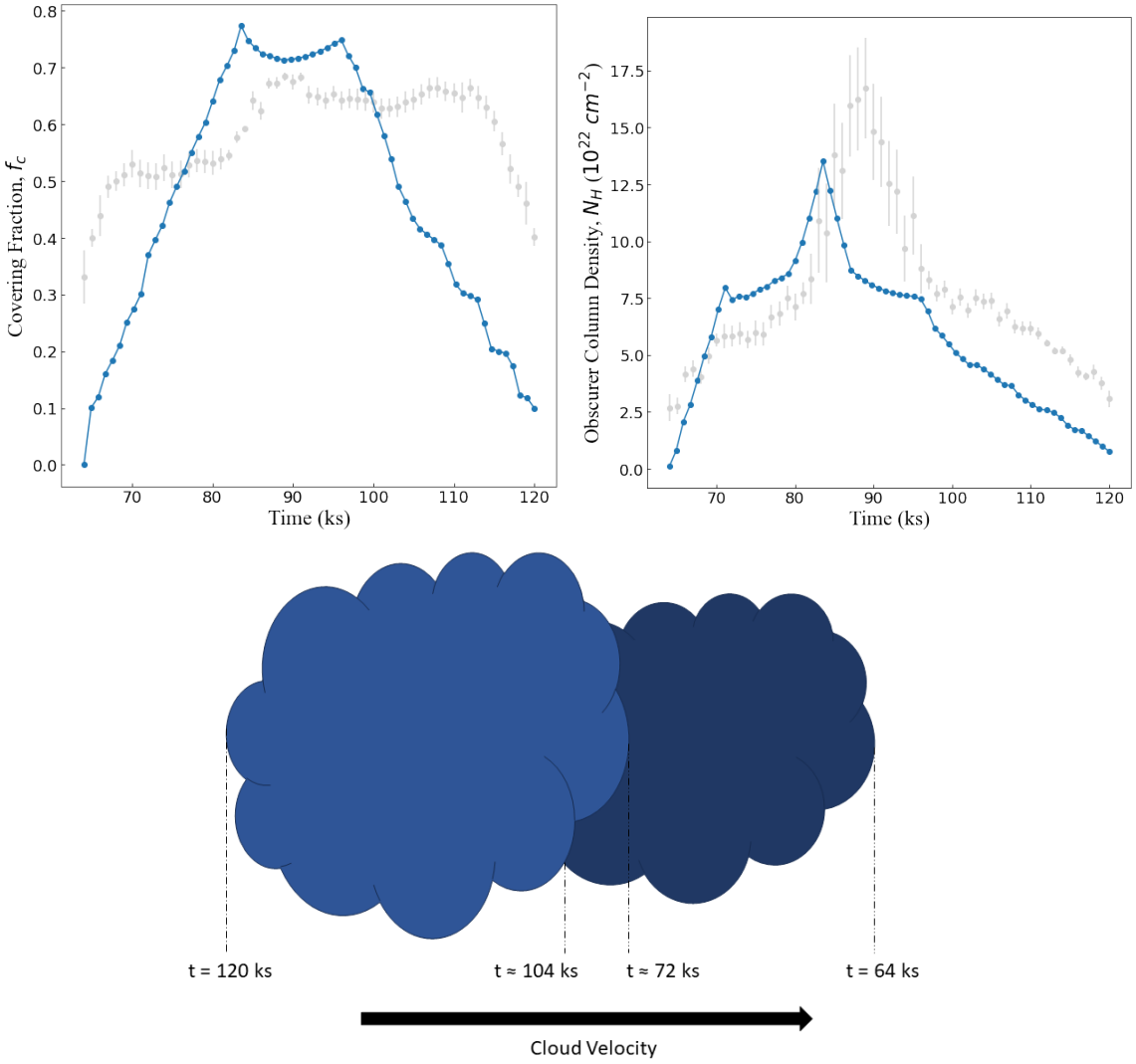

Figure 3.5: Simulation consisting of two homogeneous clouds showing the expected changes in covering fraction (**top left**) and column density (**top right**) as a function of time. The placements of the clouds in the simulation are arbitrary and will affect the overall shape of the curves. A rough sketch of the double cloud system is also presented (**bottom**), showing how it would appear while crossing our line-of-sight (direction denoted by the cloud velocity). Dashed lines indicate start and end times for both clouds. The darker shaded cloud represents a cloud with a higher maximum column density, and the relative sizes of the clouds relate to how their covering fractions compare. The first cloud (64 ks $\leq$ t $\leq$ 104 ks) varies in f_c from 0.1 to 0.7 back to 0.1, and varies in N_H from 1.0 to 21.0 back to 1.0, in units of 10^{22} cm^{-2}. The second cloud (72 ks $\leq$ t $\leq$ 120 ks) varies in f_c from 0.1 to 0.65 back to 0.1, and varies in N_H from 0.8 to 6.0 back to 0.8, in units of 10^{22} cm^{-2}.

replications of the data, but appear to be a step in the right direction compared to the simulations of a single, homogeneous cloud.

The scenario described is not strictly representative of two homogeneous clouds, but could be applied more generally. The simulations could also be replicating non-spherical and / or non-homogeneous obscurers.

3.3.2 Triple cloud

A three homogeneous cloud system that arbitrarily overlap each other is a simplification of a multi-cloud obscurer. In Fig. 3.6, we present the simulation of such a system and find it replicates the behaviour in NGC 6814 well. The addition of this third obscurer results in significant fluctuations in the parameters over time. Present in the covering fraction curve are multiple regions of flattening and two peaks. Additionally, sharp rises and drops are also evident, similar to the data. The column density curve nearly shows multiple peak, a large peak with small peaks on either side. This indicates that a multi-cloud geometry could be plausible for describing the obscurer in explaining in NGC 6814.

3.3.3 Multiple clouds in an ionised coma

The final simulation is the three-cloud system (as above), but the clouds are now embedded in a large coma or halo of highly ionised material. The ionization level of

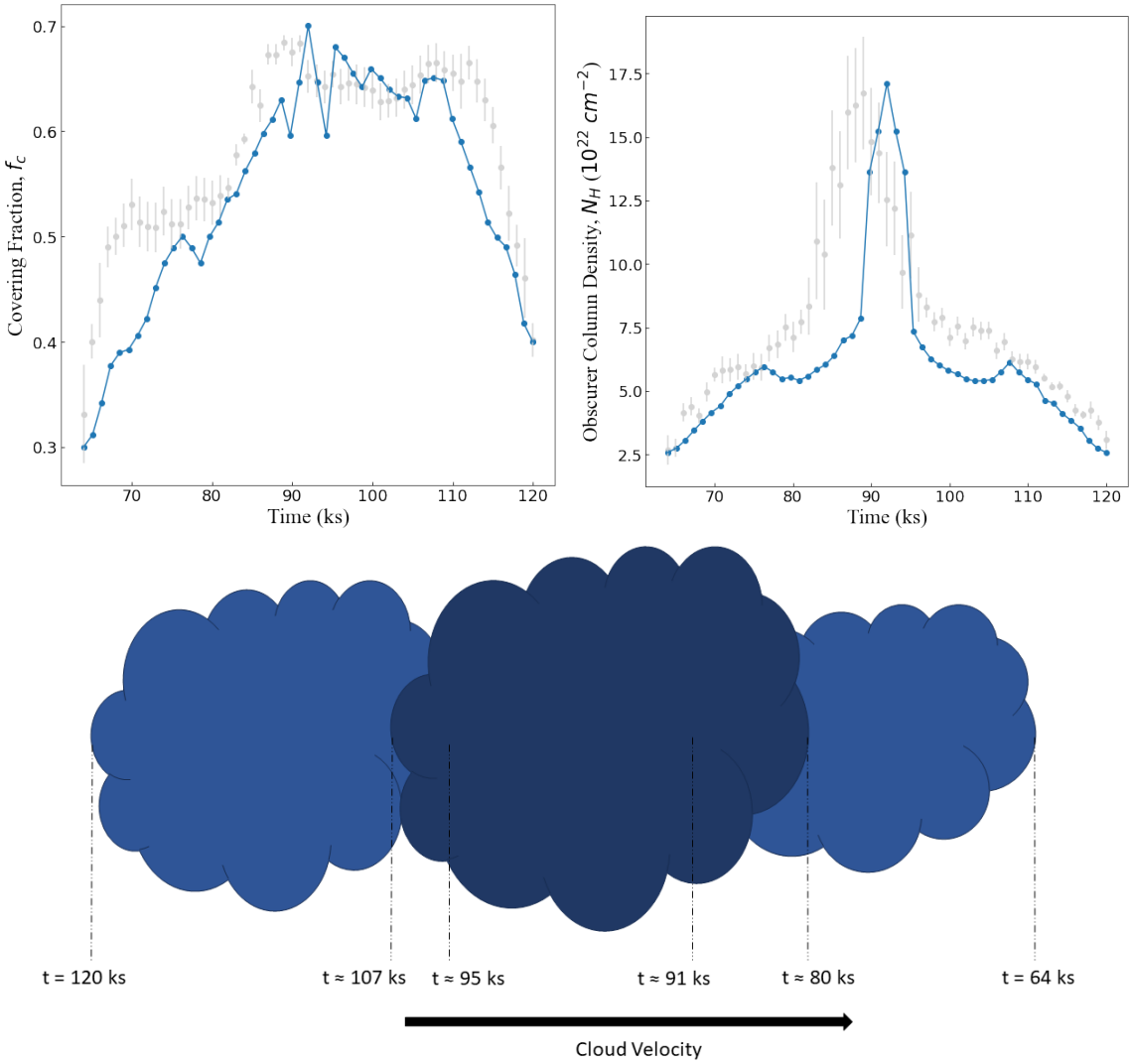

Figure 3.6: Simulation consisting of three homogeneous clouds showing the expected changes in covering fraction (**left**) and column density (**right**) as a function of time. The placements of the clouds in the simulation are arbitrary and will affect the overall shape of the curves. A rough sketch of the triple cloud system is also presented (**bottom**), showing how it would appear while crossing our line-of-sight (direction denoted by the cloud velocity). Dashed lines indicate start and end times for each of the clouds. The darker shaded cloud represents a cloud with a higher maximum column density than the other two, and the relative sizes of the clouds relate to how their covering fractions compare. The first cloud (64 ks $\leq$ t $\leq$ 91 ks) varies in f_c from 0.3 to 0.5 back to 0.3, and varies in N_H from 2.5 to 6.0 back to 2.5, in units of 10^{22} cm^{-2}. The second cloud (80 ks $\leq$ t $\leq$ 107 ks) varies in f_c from 0.1 to 0.7 back to 0.1, and varies in N_H from 5.0 to 16.0 back to 5.0, in units of 10^{22} cm^{-2}. The third cloud (95 ks $\leq$ t $\leq$ 120 ks) varies in f_c from 0.4 to 0.66 back to 0.4, and varies in N_H from 2.5 to 6.0 back to 2.5, in units of 10^{22} cm^{-2}.

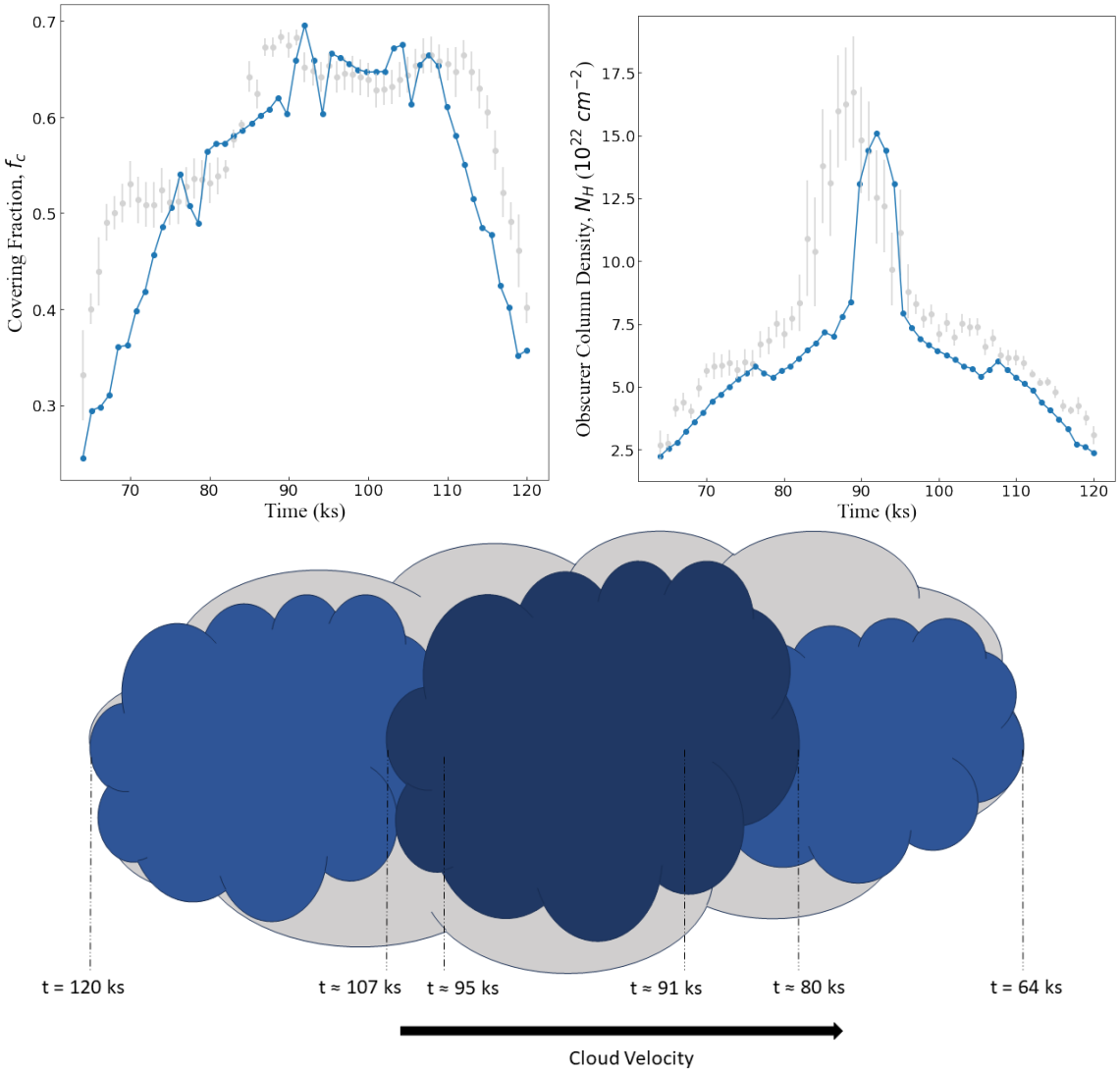

Figure 3.7: Simulation consisting of three homogeneous clouds, plus some higher ionization cloud/halo showing the expected changes in covering fraction (**left**) and column density (**right**) as a function of time. The placements of the clouds in the simulation are arbitrary and will affect the overall shape of the curves. A rough sketch of the triple cloud + higher-ionization cloud system is also presented (**bottom**), showing how it would appear while crossing our line-of-sight (direction denoted by the cloud velocity). Dashed lines indicate start and end times for each of the clouds. The darker shaded cloud represents a cloud with a higher maximum column density than the others, and the relative sizes of the clouds relate to how their covering fractions compare. The higher-ionization ($log(\xi) = 2.0$) cloud (spanning the entire time) is shown in a lighter colour than the others to distinguish it. The first cloud (64 ks $\leq$ t $\leq$ 91 ks) varies in f_c from 0.2 to 0.5 back to 0.2, and varies in N_H from 2.5 to 6.0 back to 2.5, in units of 10^{22} cm^{-2}. The second cloud (80 ks $\leq$ t $\leq$ 107 ks) varies in f_c from 0.2 to 0.67 back to 0.2, and varies in N_H from 6.0 to 17.0 back to 6.0, in units of 10^{22} cm^{-2}. The third cloud (95 ks $\leq$ t $\leq$ 120 ks) varies in f_c from 0.3 to 0.65 back to 0.3, and varies in N_H from 2.5 to 6.0 back to 2.5, in units of 10^{22} cm^{-2}. Additionally, the higher-ionization cloud spans the entire period, and varies in N_H from 0.1 to 0.6 back to 0.1, in units of 10^{22} cm^{-2}, while staying constant at f_c=0.6.

the coma is fixed at $log(\xi) = 2.0$, which is comparable to the degree of ionization found in Gallo et al. (2021). The simulation is shown in Fig. 3.7.

The differences between this simulation and the three-cloud system without the ionised coma are subtle. The distinct features in the covering fraction curve are still present, but the ingress ($t \sim 60 - 70$ ks) and egress ($t \sim 110 - 120$ ks) stages are less steep as the values are slightly larger. The main difference is in the column density curve, where the ingress and egress stages are more rounded and better replicate the observation.

The simulations demonstrate that the eclipsing obscurer in NGC 6814 was more complex than a single, homogenous cloud. Some compact, clumpy cloud system, perhaps embedded within a highly ionised coma, could describe the eclipsing in NGC 6814.

3.4 Discussion

Eclipsing events have been caught in several AGN (e.g. De Marco et al. 2020; Costanzo et al. 2022; Brenneman et al. 2013; Turner et al. 2018; Nardini & Risaliti 2011; Kaastra et al. 2014; Longinotti et al. 2013; Longinotti et al. 2019; Ebrero et al. 2016; Risaliti et al. 2007; Risaliti et al. 2011). Even though eclipses are transient, X-ray observations of them provide diagnostics of the absorbing medium and X-ray source, which is important as such regions are impossible to image with current telescopes.

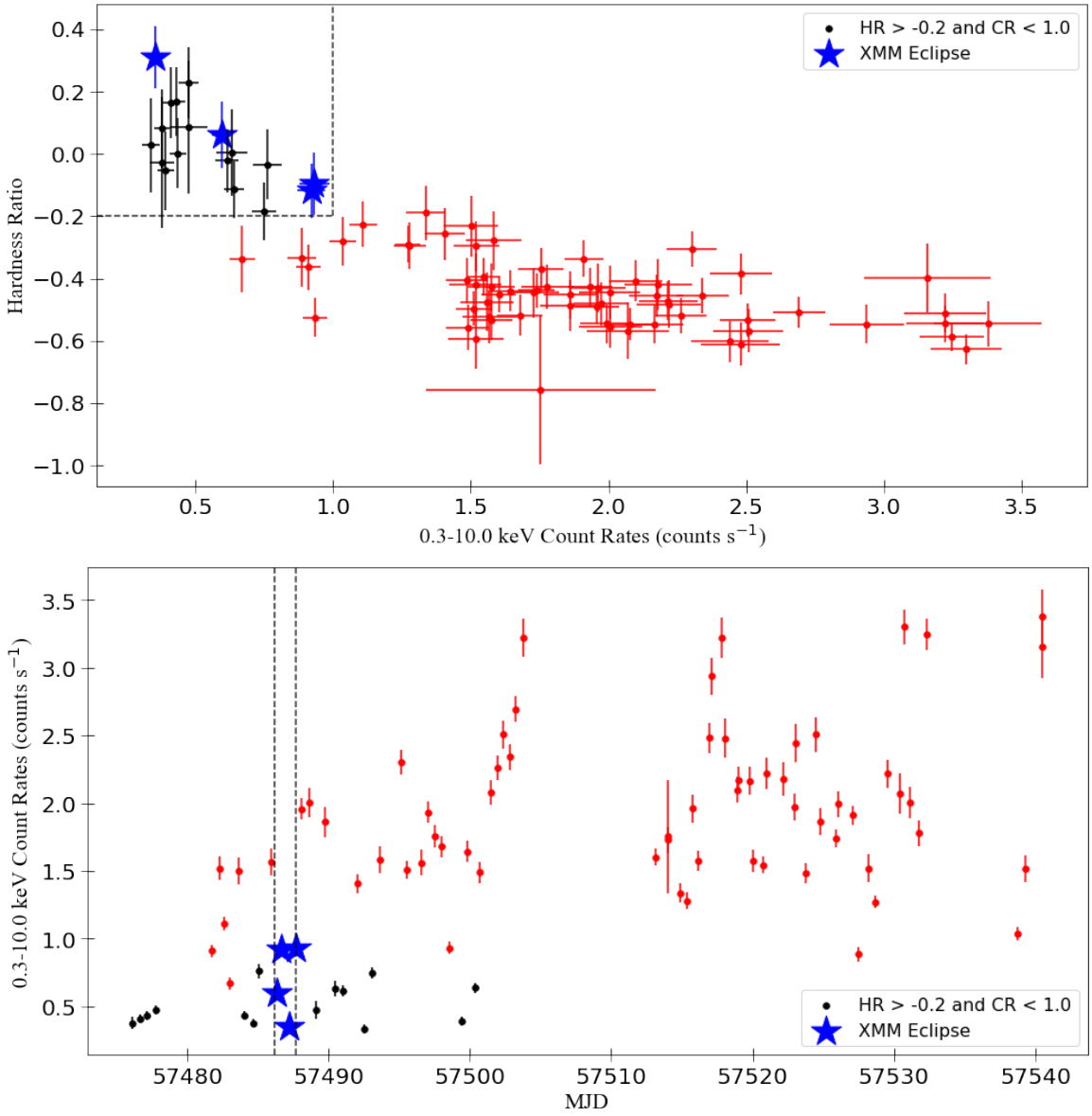

Figure 3.8: *Swift* XRT monitoring of NGC 6814 for ≈ 64 days around the time of the *XMM-Newton* eclipse. The hardness ratio (HR) as a function of count rate (CR) is shown in the top panel where data points with HR > -0.2 and CR < 1.0 are sectioned off and shown in black. The blue stars correspond to observations that occurred during the *XMM-Newton* eclipse. The points in the box meet the eclipse criteria (see text for details). For HR, the bands used are S $(0.3 - 1.0$ keV) and H $(4.0 - 10.0$ keV), with $HR = (H - S)/(H + S)$. The *Swift* XRT light curve $(0.3 - 10.0$ keV) is plotted in the lower panel. The period during the *XMM-Newton* eclipse is marked by vertical dashed-lines. Using the count rate errors from the product builder, Gaussian error analysis is used to calculate the hardness ratio errors.

In the case of NGC 6814, studying the eclipse in colour-colour space reveals complexity in the nature of the obscurer. The variation in the column density and covering fraction, both of which connect to its geometry of the obscurer passing the line-of-sight, indicate something more complicated than a simple, single cloud. We gain important information on the location and nature of the obscuring medium, which in turn helps us better understand the AGN environment and the importance of AGN winds.

The event in NGC 6814 is unique amongst eclipsing AGN, as the 2016 *XMM-Newton* observation captured the entire eclipse, which lasted about one day. *Swift* also captured the eclipse, as it observed NGC 6814 for $\sim$ 60-days over a similar time frame. The *Swift* light curve, showing the long-term variability over two-months is in the bottom panel of Fig. 3.8. The *Swift* observations occurring during the *XMM-Newton* pointing are identified as stars in the figure. The data were downloaded from the *Swift* XRT Product Builder (Evans et al. 2009)[2].

Additionally, the top panel of Fig. 3.8 portrays the *Swift* hardness ratio as a function of count rate. Again, the data coincident with the *XMM-Newton* pointing are identified with blue stars. Using the *XMM-Newton* eclipse as a baseline, we can establish an eclipse criteria. The verified *XMM-Newton* eclipse is clearly distinguished with the criteria of HR $>$ -0.2 and CR $<$ 1.0 (sectioned off by the dashed lines). In addition, high-cadence observations of NGC 6814 in 2022 indicate that HR< -0.2 are

[2]`https://www.swift.ac.uk/user_objects/`

consistent with the unobscured state of the AGN (Gonzalez et al. 2024).

Based on the established hardness ratio – count rate criteria, there are several points (black points in Fig. 3.8) in the $\sim$ 2 month *Swift* light curve that resemble the behaviour during the eclipse suggesting there may have been several obscuring events in 2016. All these events occur in the $\sim$ 30 days prior to MJD = 57505. Based on previous reports about NGC 6814 (e.g. Gallo et al. 2021; Leighly et al. 1994), eclipses in this source may not be uncommon, which is further supported by the possibility that these fluctuations indicate it being prone to more eclipses during the 2016 epoch. If the black points in Fig. 3.8 are associated with eclipses, this would imply a large covering factor of the sky as seen from the black hole.

With this eclipse criteria in mind, we can get an idea of the number of obscuring clouds in the line-of-sight during the *Swift* observation. Finding the occasions when the data suggest the onset and end of an eclipse (i.e. shifting from red to black to red data points), we identify about 6.5 possible eclipsing events. Since the first event occurs right at the beginning of the light curve, and it only shows an increase, it is possible that this is not a full eclipsing event, thus, we consider it half of an eclipse. Using this information, and the fact that various properties of the partial coverer were calculated in Gallo et al. (2021), we can estimate the fraction for the occurrence of these events, both throughout the Swift observation and the period of heavy eclipsing activity (before the gap at MJD = 57505 days of Fig. 3.8).

From Gallo et al. (2021), the Keplerian velocity of the partial coverer was calculated to be $V_K = 10^4$ km s^{-1}, the location of it was calculated to be $r = 2694\ r_g = 4.34 \times 10^{15}$ cm. This results in an orbital pathlength of $C = 2\pi r = 2.73 \times 10^{16}$ cm, and an orbital period (Keplerian timescale) of $T_K = C/V_K = 27269$ ks. The duration of the entire *Swift* light curve is $t_{lc} \sim 64$ days $= 5529.6$ ks, which covers approximately 0.2 of the Keplerian orbit.

The estimated diameter of the cloud was calculated to be $D_C = 1.30 \times 10^{13}$ cm. Assuming all the cloud sizes are similar and that there are 6.5 eclipsing events, the total distance (arc length) covered by the clouds would be $D_{tot} = 6.5\ D_C = 8.45 \times 10^{13}$ cm. Based on this, the fraction of the orbit covered by clouds is ≈ 0.015.

All the events occur prior to MJD = 57505 days. The duration of the *Swift* light curve during this phase is $\sim$ 27 days = 2332.8 ks, corresponding to approximately 0.086 of the Keplerian orbit. The orbital covering factor during this heavy-obscuration phase is ≈ 0.036. The *Swift* light curve suggests that eclipses in NGC 6814 are likely and that the distribution of clouds in the orbit is not isotropic.

In the original paper, Gallo et al. (2021) modelled the spectra during the high, ingress, low, and egress states. The uniform light curve and time-resolved spectroscopy were indicative of a single cloud transiting the X-ray source. As the analysis was mainly spectroscopic, time resolution was sacrificed for signal-to-noise. With the colour-colour analysis here, we can examine the transit with much better time resolu-

tion. With the ability to examine the obscurer during the deepest part of the eclipse, we find that the obscurer may be inconsistent with a single homogeneous cloud. As seen in Fig. 3.4, the changes in both f_C and N_H are not symmetric, which is what would be expected for a uniform obscurer such as a single cloud. Moving in this direction by testing various scenarios, it appears that the transit can be described by multiple clouds moving together. This scenario (as depicted in both Fig. 3.6 and Fig. 3.7) reproduces the f_c and N_H behaviour.

The colour-colour analysis can be used to reveal details about the obscuring medium. For NGC 6814, the obscuring is either inhomogeneous or substantially fragmented into many pieces. A recent reverberation mapping study from a 2022 X-ray-to-optical monitoring campaign (Gonzalez et al. 2024) suggests that the outer disc is truncated at a smaller radius than is normally expected in such AGN. This indicates a potential source for the obscuring material originating much closer to the black hole and might imply a higher rate of eclipses in NGC 6814 and the presence of inhomogenous material.

3.5 Conclusion

In this chapter, we have used colours to examine the eclipsing event in NGC 6814. We have found that these data exhibit absorption variability consistent with changes in both obscurer covering fraction and column density. These variations are inconsis-

tent with what would be expected from a single, homogeneous cloud. Rather, more complex simulations showed that it is likely due to multiple clouds moving together.

Long-term, high cadence monitoring of NGC 6814 would be useful to determine how common such eclipses are in the AGN. This would reveal the nature and origin of the obscurer(s) causing the eclipses. Additionally, this work could lead to better identifying eclipses in AGN, and characterising the behaviour of the obscurers.

Chapter 4

Studying the Brightness Dip in Zw 229.015

4.1 Introduction

While, in Chapter 3, we have just discussed absorption variability in the form of an eclipse, there are other ways in which light curves can be seen to vary. The spectra give clues for what form of variability may be occurring based on how the spectra change in different energy bands. These changes mostly arise from changes in the accretion disc or corona.

Coincident X-ray and UV variability can either be due to reprocessing of coronal

X-ray photons by the accretion disc, where the source of variability is the corona, or through changes in the accretion disc propagated into the X-ray due to Comptonisation via the corona. A change in the disc accretion rate ($\dot{m}$) modifies the production of seed UV photons, which would manifest itself in changes in the amount of UV photons that are Comptonised by the corona. Changes in the level of Comptonisation in the corona will manifest in parameters like the photon index. Different cases of variability not related to absorption have been seen in the BAT 58-month survey (many AGN in the survey have variability consistent with coronal variations; Soldi et al. 2014).

In determining the origin of variability, various timescales related to the accretion disc and black hole must be explored. Different types of variability are governed by the timescales of the different processes associated with them.

In general, the dynamical timescale (t_{dyn}) is the time it takes for a certain change to occur because of particle movement. It is essentially an orbital timescale. In the context of AGN, this timescale can be applied to the accretion flow. This timescale describes various parts of the disc, like rotation at different distances from the black hole (Czerny 2006):

$$t_{dyn} = 500\left(\frac{M_8}{M_\odot}\right)\left(\frac{r}{r_g}\right)^{3/2} sec \tag{4.1}$$

Here, M_8 is the mass of the black hole in units of $10^8 M_\odot$, and r is the radial distance from the black hole in units of r_g.

Next, there is the thermal timescale (t_{th}). As the name suggests, this timescale is related to temperature changes (i.e., heating and cooling) in the disc. It includes the dimensionless disc viscosity parameter, α (Equation 4.2), that is a measure of the stress compared to the pressure in the disc.

$$t_{th} = \frac{t_{dyn}}{\alpha} \tag{4.2}$$

Then, there is the viscous timescale (t_{vis}). This timescale, generally defined as a ratio of the radius to the radial velocity, describes the flow of mass in an accretion disc (Equation 4.3):

$$t_{vis} = t_{th}\left(\frac{r}{h_d}\right)^2 \tag{4.3}$$

where h_d is the disc height.

The time for light to cross some distance (r) is the light crossing time (t_{cross}):

$$t_{cross} = \frac{r}{c} \tag{4.4}$$

Comparing the variability timescales observed in AGN light curves to these predicted time scales in a standard accretion disc can provide insight to the physical processes at work in AGN.

4.2 Observations and Data Processing

Throughout the work on Zw 229.015, we focus on Swift observations spanning from 2009 to 2018, involving both X-ray (XRT) and UV (UVOT) data. Due to the range of years for the Swift observations, we are presented with useful multi-epoch data and long time lines.

All of the observations can be seen in Table 4.1. Spanning about 9 years, Swift observed Zw 229.015 with XRT for a total of 78 observations (5 of which were not processed due to data issues), while simultaneously employing the use of the various filters on the UVOT.

To analyze these observations, data were retrieved and processed, as outlined here. The X-ray data are retrieved using the Swift XRT Product Builder[1], while the UV data are downloaded from the Swift archive and processed. Light curves and spectra were created from the Swift XRT product builder, covering all Swift observations of Zw 229.015. For the light curves, binning was by ObsID, meaning one light curve data point per observation, over the 0.3-7.0 keV range. Time is given in units of MJD. The total light curve is shown in Fig. 4.1.

In Fig 4.1, between days 710 and 770, there is a curious dip in the brightness that is similar to the light curve of NGC 6814 (Fig 3.1). Of interest, is if this brightness dip is also due to an eclipsing event. The data between 710 and 770 corresponds

[1] `https://www.swift.ac.uk/user_objects/`

Table 4.1: Table of the Zw 229.015 Swift observations used in this work. The "..." between different rows indicates other observations in that sequence of observation IDs (of the same target ID).

(1) Observation ID	(2) Start Date (yyyy-mm-dd)	(3) XRT Exposure (s)	(4) UVOT Exposure (s)
00090185001	2009-06-18	5065	5065
00039852001	2009-07-07	7672	6664
00039852002	2009-07-10	3536	3535
00041246001	2011-01-26	1743	1740
00041246002	2011-07-03	1013	1012
00041246003	2011-07-04	1133	1132
...	...	...	...
00041246019	2011-07-21	241	239
00041246020	2011-07-22	933	932
00041246021	2020-11-29	3029	2952
00091030001	2011-05-29	1193	1192
00091030002	2011-05-30	908	867
00091030003	2011-05-30	1253	1252
...	...	...	...
00091030047	2011-06-30	1397	1354
00091030048	2011-07-01	1276	1273
00091030049	2011-07-02	1108	1107
00048585001	2012-08-19	1101	1099
00048585002	2012-08-23	712	711
00081228001	2018-02-11	7170	7108

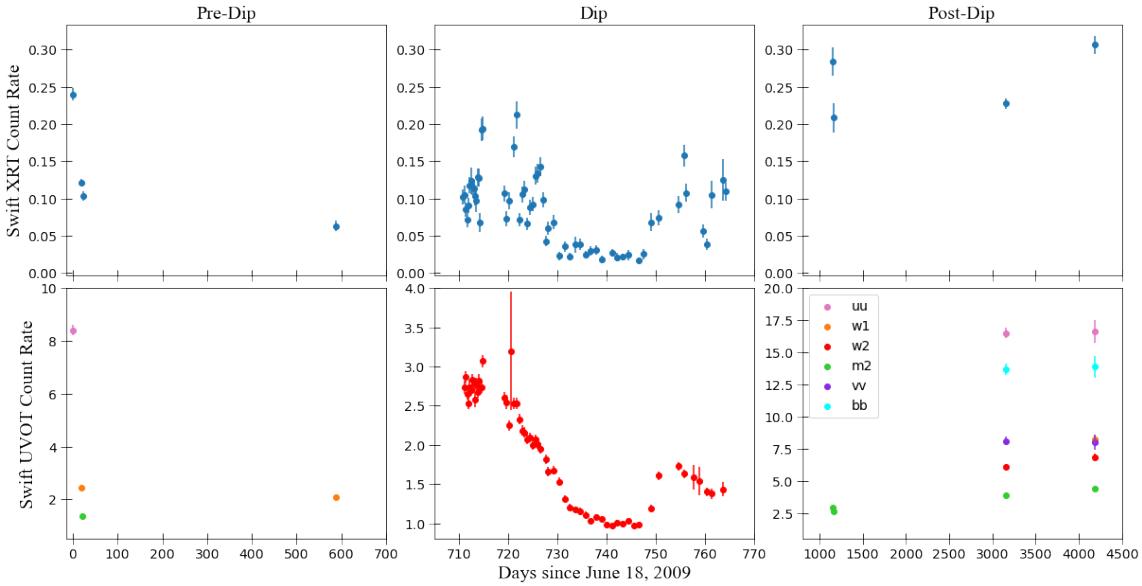

Figure 4.1: The Swift (XRT and UVOT) light curves for Zw 229.015. The X-ray data (XRT) are shown in the top panels in blue, and the UV data (UVOT) are shown in the bottom panels. Each of the UV filters are indicated by different colours: B (light blue), V (purple), U (pink), UVM2 (lime green), UVW1 (orange), and UVW2 (red). To focus in on the dip better, we split the light curve into three side-by-side panels. We also indicate how we divided the data into the three epochs via the titles for each plot column, with the left panels denoting the pre-dip epoch, middle panels denoting the dip epoch, and right panels denoting the post-dip epoch.

roughly to the minimum brightness phase we call the dip. The pre-dip and post-dip data occur before 710 and after 770, respectively, when the brightness of Zw 229.015 seems rather typical.

Time-averaged X-ray spectra are created specifically for these three epochs of interest using the Swift XRT product builder. Output spectral files are then retrieved from the site using the appropriate Job ID. These are optimally binned in XSPEC.

Using the Swift archive[2], all observations with the UVOT are selected and files to be processed are downloaded. These data are processed using the following processing steps, to get UV light curves and spectra. For each observation, we select a circular source region (5" centered on the source) and a background region (15" off-source), which are used on the images. Then, a UV processing script, provided by Adam Gonzalez, is run to create various files, including data files and fits files. The fits files contain various parameters, including count rates, flux densities (in Jy), and times for the light curve. To create UVOT spectra, the flux densities are averaged over the epochs of interest for each of the available filters. For the pre-dip epoch, UVOT spectra include the U, UVW1, and UVM2 filters. During the dip, only the UVW2 filter is used. Post-dip uses the U, V, B, UVM2, UVW1, and UVW2 filters. These fluxes for each epoch and each filter are then passed through the FTFLX2XSP tool, which creates appropriate spectral response files that can be used in XSPEC. The X-ray and UVOT spectra at each epoch is shown in Fig. 4.2.

[2]`https://swift.gsfc.nasa.gov/archive/`

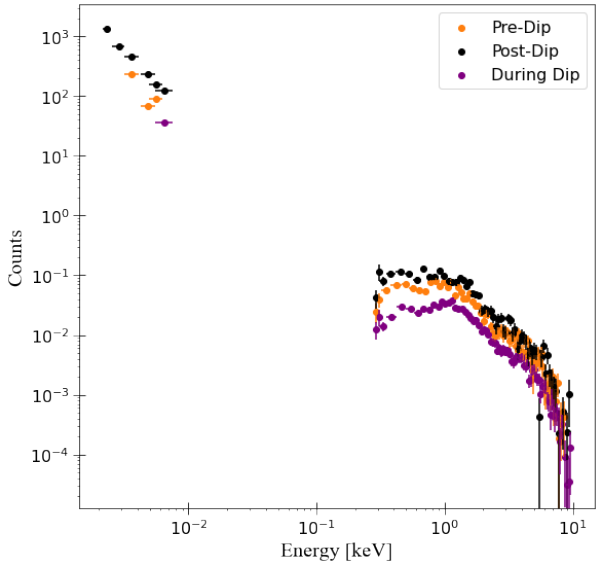

Figure 4.2: The Swift spectra for Zw 229.015 in the pre-dip, post-dip, and dip epochs are shown in orange, black, and purple, respectively.

4.3 Light Curves and Spectral Analysis

Figure 4.1 shows light curves for Zw 229.015. It shows both the Swift XRT (top panels) and Swift UVOT (bottom panels) light curves. The dip (shown in the middle panels) occurs during mid-June of 2011, and is evident in both the XRT (top middle) and UVOT (bottom middle) light curves. While the flux changes happen simultaneously in time, there are differences in the shapes of the dips. The UV dip starts more gradually than the X-ray dip, but both dips coincide well with each other.

Other than between $\sim$ 710 and 770 days since June 18, 2009, the data are quite remarkably smooth, with little to no variability. Although, there is very little data during these periods. During the dip shown in the Swift data, there are no extra bumps

that would usually indicate more intricate variability (i.e., it is a rather smooth dip). There is a gap in the Swift data between $\sim$ 715 to 720 days, but it is mostly filled in by XMM data, however we do not analyze that here.

Spectra for these three epochs demonstrate the changes between epochs (Fig. 4.2). From first look, it appears as if there are mostly normalization changes, where the spectrum changes in brightness, but not necessarily in shape. This is probably not due to absorption, like in NGC 6814 (Chapter 3), which would induce significant curvature in the X-ray spectrum depending on column density.

To test, we attempted spectral fits with different types of absorption (e.g. partial covering, dust extinction, and gas photoelectric absorption) and without absorption. The underlying continuum was modelled with the Comptonisation scenario (see Section 1.1.3) in mind, with the inclusion of disc, hot corona, and warm corona components. Studies such as Tripathi et al. (2019) have favoured this interpretation. All fits will also include a host galaxy component (Sased) and a Balmer continuum component (BalmerCont). These components are non-variable over the observed timescales and can be linked over the epochs.

When reporting the fit quality we use the Akaike Information Criterion (AIC) (AIC = 2k - 2ln($\mathcal{L}_{ML}$); Tan & Biswas 2012). In particular, we use the corrected version, AIC$_C$. The small amount of UV data, but comparably larger amount of X-ray data leads to us using χ^2 for the UV, but C-stat for the X-ray. To properly assess

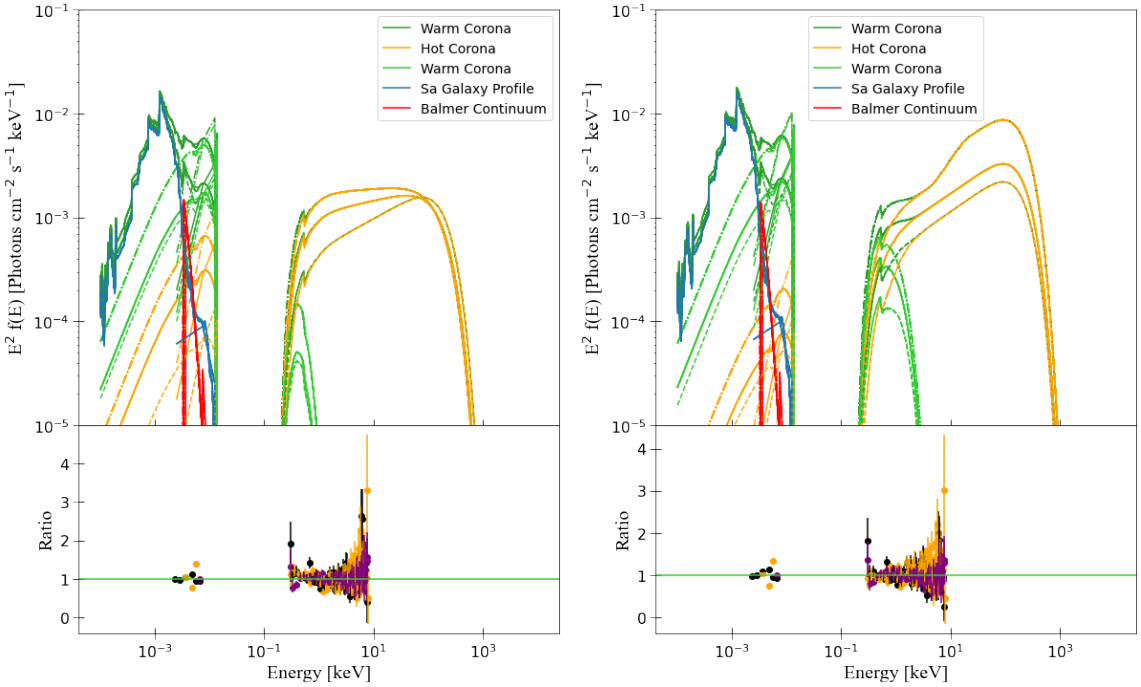

Figure 4.3: Plots showing the fits for the models. The top panels show the SEDs from each model and the bottom panels show the residuals for each model. On the left is the continuum variability model (Table 4.2) and on the right is the partial covering model (Table 4.3). The different coloured lines on the SED plot indicate which components contribute to different parts of the SED. Green and lime green represent contributions from the warm corona model, orange represents the contribution from the hot corona model, blue represents the contribution from the galaxy profile, and red represents the contribution from the Balmer continuum, with different linestyles being used to represent the different epochs: pre-dip (solid line), dip (dashed line), and post-dip (dash-dotted line). In the bottom panels, the epochs are represented by different colours: pre-dip (orange points), dip (purple points), and post-dip (black points).

the total fit, while also not having to directly note the degrees of freedom (d.o.f.), we describe the fit using AIC_C. This corrected version is used for smaller data sets and adds a correction term: $\frac{2k(2k+1)}{N-k-1}$. Note that $(\mathcal{L}_M L)$ is the maximum likelihood and corresponds to the likelihood when evaluated with the parameters that maximize it. When calculated for the maximum likelihood parameters, the total fit statistic (we will call it T) can be expressed in the following way: $\mathcal{L} \propto e^{-T/2}$. The equation used to calculate AIC_C is shown in Equation 4.5, where n is the number of data points being fit, and k is the number of free parameters in the evaluated model (Tan & Biswas 2012).

$$AIC_C = 2k + T + \frac{2k^2 + 2k}{n - k - 1} \tag{4.5}$$

Preliminary fits did not require the disc component. This can occur if the warm corona extends over a sufficiently large portion of the disc as to reduce the direct component we measure (Petrucci et al. 2020). Consequently, from this point onward, we assumed a hot corona and a warm corona (both using NTHCOMP) and tested two scenarios to describe the origin of the brightness dip in Zw 229.015: variations in corona parameters and variations in parameters of some partial coverer (using ZXIPCF). The fits for the former are shown in Table 4.2 and the left panels of Fig. 4.3, and the fits for the latter are shown in Table 4.3 and the right panels of Fig. 4.3.

The fit quality between the two scenarios are quite similar (AIC_C = 517.19 and

518.85, respectively), however the parameters of the former are perhaps more reasonable. In the former scenario, intrinsic changes in the power law components are responsible for the observed variability (Table 4.2). The hot corona changes in both brightness (normalisation) and shape (Γ), becoming flatter as it dims. This flatter-when-dimmer behaviour is well known (Yang et al. 2015). The warm corona also changes in brightness as reflected in the constant scaling parameter in the fit, while its shape does not clearly vary. Overall, the parameters are seen to be quite reasonable, with Γ_{warm} fitting, within uncertainties, to typical AGN values (Petrucci et al. 2018). What is also seen to change between the bright and dim states is the relative contribution of the hot and warm coronae. From pre-dip to the dip, the brightness of the hot corona drops from $\approx 50\%$ to 30% that of the warm corona. Overall, the dimming in Zw 229.015 can be interpreted as arising from considerable dimming of the hot corona.

The second scenario examined if the brightness dip could arise from changes in a partial coverer passing along the LOS, like in NGC 6814 (Chapter 3), instead of intrinsic AGN changes (Table 4.3). Here, we allow the warm corona to vary by a constant scaling factor, but the variations in the hot corona are due to a covering cloud. The resulting fit is statistically equivalent ($\mathrm{AIC}_C = 518.85$) to the intrinsic variable corona model, however the behaviour is difficult to understand. Notably, the column density is highest ($\approx 5 \times 10^{23}$ cm^{-2}) in the post-dip epoch, but negligible

Table 4.2: Table for fit parameters in the continuum variability scenario, with errors taken as the 68% confidence limits from a MCMC run. In XSPEC terminology, the model used is: REDDEN*PHABS*(NTHCOMP + CONSTANT*NTHCOMP + ATABLE(SASED) + ATABLE(BALMERCONT)).

Model Component	Model Parameter	Pre-Dip	During Dip	Post-Dip
REDDEN	E(B-V)	0.075		
PHABS	$N_H/10^{22}$ cm^{-2}	0.0743		
NTHCOMP$_{hot}$	Γ_{hot}	$1.87^{+0.04}_{-0.04}$	$1.71^{+0.03}_{-0.03}$	$1.93^{+0.04}_{-0.04}$
	kT$_e$/keV	100.00		
	kT$_{bb}/10^{-3}$ keV^{-1}	$2.68^{+0.45}_{-0.34}$		
	norm$/10^{-3}$	$1.09^{+0.03}_{-0.03}$	$0.50^{+0.01}_{-0.01}$	$1.66^{+0.05}_{-0.05}$
CONSTANT	factor	$0.35^{+0.02}_{-0.02}$	$0.28^{+0.01}_{-0.01}$	1.00
NTHCOMP$_{warm}$	Γ_{warm}	$2.66^{+0.12}_{-0.13}$		
	kT$_e$/keV	$0.12^{+0.03}_{-0.02}$		
	kT$_{bb}/10^{-3}$ keV^{-1}	$2.68^{+0.45}_{-0.34}$		
	norm$/10^{-5}$	$2.14^{+2.27}_{-1.10}$		
ATABLE(SASED)	norm$/10^{-18}$	$6.22^{+0.61}_{-0.62}$		
ATABLE(BALMERCONT)	T$_e$/keV	8000		
	norm$/10^{-3}$	$3.13^{+0.39}_{-0.37}$		
	Hot/Warm	0.47	0.29	0.69
Fit Quality	AIC$_C$	517.19		

Table 4.3: Table for fit parameters in the partial covering variability scenario, with errors taken as the 68% confidence limits from a MCMC run. In XSPEC terminology, the model is: ZXIPCF*REDDEN*PHABS*(CONSTANT*NTHCOMP + CONSTANT*NTHCOMP + ATABLE(SASED) + ATABLE(BALMERCONT)).

Model Component	Model Parameter	Pre-Dip	During Dip	Post-Dip
ZXIPCF	$N_H/10^{22}$ cm^{-2}	$0.05^{+0.01}_{-0.00}$	$0.30^{+0.19}_{-0.08}$	$45.37^{+58.01}_{-16.74}$
	$\log(\xi)$	$-0.73^{+0.24}_{-0.23}$		
	f_C	$0.11^{+0.10}_{-0.05}$	$0.51^{+0.09}_{-0.06}$	$0.41^{+0.03}_{-0.02}$
REDDEN	E(B-V)	0.075		
PHABS	$N_H/10^{22}$ cm^{-2}	0.0743		
NTHCOMP$_{hot}$	Γ_{hot}	$1.65^{+0.06}_{-0.09}$		
	kT$_e$/keV	100.00		
	kT$_{bb}/10^{-3}$ keV^{-1}	$3.22^{+0.56}_{-0.42}$		
	norm$/10^{-3}$	$1.98^{+0.16}_{-0.24}$		
CONSTANT	factor	$0.38^{+0.01}_{-0.01}$	$0.25^{+0.01}_{-0.01}$	1.00
NTHCOMP$_{warm}$	Γ_{warm}	$2.48^{+0.06}_{-0.05}$		
	kT$_e$/keV	$0.30^{+0.06}_{-0.03}$		
	kT$_{bb}/10^{-3}$ keV^{-1}	$3.22^{+0.56}_{-0.42}$		
	norm$/10^{-3}$	$0.88^{+0.29}_{-0.16}$		
ATABLE(SASED)	norm$/10^{-18}$	$6.94^{+0.59}_{-0.69}$		
ATABLE(BALMERCONT)	T$_e$/keV	8000		
	norm$/10^{-3}$	$2.95^{+0.37}_{-0.36}$		
Fit Quality	AIC$_C$	518.85		

($< 10^{22}$ cm^{-2}) during and before the dip. If this were the source of the variability, it would be expected that the column density and covering fraction would both be largest during the dip. Therefore, this scenario seems extremely unlikely.

4.4 Discussion

Spectral modelling shows that Zw 229.015 does not require any disc component, but does require two power laws (representing hot and warm coronae). The spectral

variability cannot be explained by obscuration changes, but can be explained by continuum changes, such as coronal variations. In the non-absorption model, the data can be explained with changes in the brightness of both coronae, and the shape of the hotter one. The AIC_C values between the two models are very similar, with the coronal variation model having $\mathrm{AIC}_C = 517.19$, and the partial covering model having $\mathrm{AIC}_C = 518.85$.

The best partial covering fit represents an unlikely scenario, where the column density increases out of the dip, and the covering fraction only moderately decreases out of the dip. The best fit without partial covering shows a more likely scenario, where decreases in the photon index of the hot corona coincide with dips in brightness, and the values are reasonable for such an AGN.

In the best-fit model, Zw 229.015 exhibits little disc emission, or has much of it drowned out. This posits a scenario where the disc experiences a large covering factor by the warm corona. Above ≈ 2 keV, the continuum is dominated by the hot corona, which is likely a compact region centrally located close to the black hole.

Based on the light curves, the characteristic timescale that we are interested in describing is the time it takes for Zw 229.015 to fade and brighten (i.e., ingress and egress) from the high-flux to the low-flux state. In Fig 4.1, this variability timescale in the UVW2 filter (1650 Å - 2250 Å) is about 10.8 days during the ingress and 9.0 days during the egress. Therefore, our characteristic timescale of interest is approximately

10 days.

As described in Chapter 4.1, variability can be driven by different processes occurring on different timescales. Here, we consider those timescales, specifically for Zw 229.015. In a standard accretion disc, there is a predicted relationship between the disc temperature and radius. The origin of the thermal radiation creating a certain wavelength of light can be determined by (Gallo et al. 2018):

$$\frac{r}{r_g} = (1.28 \times 10^{11})\lambda^{4/3} M_8^{-1/3} \dot{m}^{1/3} \left(1 - \sqrt{\frac{r_{isco}}{r}}\right)^{1/3} \tag{4.6}$$

where λ is the emission wavelength in metres, M_8 is the black hole mass in units of 10^8 $M_\odot$, $\dot{m}$ is the accretion rate in units of $\dot{M}_{Edd}$, r_{isco} is the radius corresponding to the innermost stable circular orbit, and r is in units of r_g.

For Zw 229.015, M = 10^7 $M_\odot$ (Tripathi et al. 2019) and $\dot{m} = 10^{-0.9} = 0.1259$ (Tripathi et al. 2019). For a black hole spin of a=0.5 (Tripathi et al. 2019), $r_{isco} = 4.23$ r_g (Netzer 2013). Based on Equation 4.6, the UVW2 (1650 Å - 2250 Å) emission is originating from about 116-179 r_g. The light crossing time at this distance is $t_{cross} = 1.6039 - 2.4617$ hours (Equation 4.4).

From Equation 4.1, we estimate the dynamical timescale at this distance to be on the order of 0.7 - 1.4 days. This is much too short to explain the characteristic timescale we observe.

For the thermal timescale (Equation 4.3), we assume a value for the viscosity

parameter of $\alpha = 0.1$ (Edelson et al. 2014). This leads to an UV thermal timescale of $t_{th} = 7.2834 - 13.8487$ days, which matches our characteristic timescale of ≈ 10 days very well.

For the viscous timescale (Equation 4.3), we follow Edelson et al. (2014), and use a disc height, h_d, that is 10% of the size scale ($r/h_d = 10$). This results in an UV viscous timescale of $t_{vis} = 1.9941 - 3.7916$ years, which is much too long compared to our data.

The calculated thermal timescale is most in-line with the observed variability timescales in Zw 229.015, seen during both ingress and egress. It fits that the UV brightness drop (dip) is due to a thermal process. To speculate, it could be that some cold spot is moving its way through the disc and mixing with material at this distance. Unfortunately, we do not have observations with other filters to potentially track this cold spot.

This behaviour is also seen in the X-rays (Fig. 4.1), which are not created by the disc. This means the variations in the disc are somehow propagated in the coronae. It is probably not the case that variability in the corona instigates the changes in the UV. The dominant variability timescale in the corona is the light crossing time. For a corona size of about 10-20 r_g, this corresponds to changes on timescales of minutes.

Chapter 5

Conclusion

In this work, we have probed the brightness dips seen in the light curves of two AGN, NGC 6814 and Zw 229.015. In both cases, the change in brightness from high to low, and back to high, follows a smooth symmetric curve that is reminiscent of exoplanet transient light curves. On the other hand, while the transition in NGC 6814 occurred over 1 day (Fig. 3.1), the event in Zw 229.015 happened over ≈ 50 days and was seen in X-ray and UV (Fig. 4.1).

In NGC 6814, the behaviour was reported to be the cause of an eclipsing event by a single, homogeneous obscuring gas cloud (Gallo et al. 2021). In this work, we revealed great complexity in the obscurer. Using a colour-colour analysis, we found that the time-resolved variations in both covering fraction and column density could only be achieved with a more complex system of multiple clouds (Chapter 3; Pottie

et al. 2023). Not only has this been shown in our work, it has also been shown in the work by Kang et al. (2023). They find a different, but equally complex obscurer that includes a collection of Compton-thick clouds. Based on estimations of various distance scales within the central engine, it was determined that these events could be rather common in NGC 6814.

Zw 229.015, while showing similar behaviour, has dips in both the X-ray and UV light curves. This generally points to changes not related to absorption, motivating the study. Analysis of the flux-resolved spectra shows that a Comptonisation scenario is favoured and that absorption is unlikely as an explanation for the variability. Timescales associated with various accretion disc processes indicate the variability is linked with a thermal timescale. This could manifest itself as some cold spot in the disc, moving its way through. This would lower seed photon production, which would then alter the X-ray photons produced via Comptonisation (Chapter 4).

Comparing NGC 6814 and Zw 229.015, there are interesting details to note. Even with similar transient-like events in the light curves of both sources, there are different explanations for the observed brightness variations. In NGC 6814, there are only variations in the X-ray, and these variations are not due to continuum variability, but instead due to absorption. With Zw 229.015, there are correlated variations in both the X-ray and UV. The behaviours of both of these light curves are likely explained by continuum variations, through changes in the accretion disc that are propagated

into the coronae. Analyses of both NGC 6814 and Zw 229.015 included some form of timescale analysis. The NGC 6814 study used the Swift light curve to estimate the occurrence of eclipsing events in the AGN. With Zw 229.015, the crossing, dynamical, thermal, and viscous timescales were compared to the light curve, leading to the determination that some thermal processes should be the cause of the variability.

Future work on Zw 229.015 would involve focusing more specifically on the middle panel of Fig. 4.1. The work in Chapter 4 adopted on a simple model to describe the spectrum, but application of a more physical model that self-consistently describes the emission from the disc and corona will be important. Colour-colour grids have proven themselves to be useful in NGC 6814 when analyzing obscuration. Applications of such grids to Zw 229.015 could be informative. This would also test how effective colour-colour grids are at quantifying continuum variability. Bayesian blocks could be employed to find similar objects. We briefly tested this on the Zw 229.015 light curves and we were able to nicely section off the start and end of the low-state. Finally, since we have predicted that the UV variations are propagating to X-ray variability, a reverberation analysis to search for time lags between the UV and X-ray would be worthwhile (e.g., Gonzalez et al. 2024).

Bibliography

Adegoke O., Rakshit S., Mukhopadhyay B., 2017, MNRAS , 466, 3951

Alston W. N., et al., 2020, Nature Astronomy, 4, 597

Arnaud K. A., 1996, in Jacoby G. H., Barnes J., eds, Astronomical Society of the Pacific Conference Series Vol. 101, Astronomical Data Analysis Software and Systems V. p. 17

Barth A. J., et al., 2011, ApJ , 732, 121

Barvainis R., 1987, ApJ , 320, 537

Bentz M. C., Katz S., 2015, PASP , 127, 67

Bianchi S., Piconcelli E., Chiaberge M., Bailón E. J., Matt G., Fiore F., 2009, ApJ , 695, 781

Blandford R. D., Payne D. G., 1982, MNRAS , 199, 883

Blandford R., Meier D., Readhead A., 2019, ARA&A , 57, 467

Blustin A. J., Page M. J., Fuerst S. V., Branduardi-Raymont G., Ashton C. E., 2005, , 431, 111

Brenneman L. W., Risaliti G., Elvis M., Nardini E., 2013, MNRAS , 429, 2662

Carini M. T., Ryle W. T., 2012, ApJ , 749, 70

Carpano S., Wilms J., Schirmer M., Kendziorra E., 2005, , 443, 103

Chainakun P., Young A. J., 2017, MNRAS , 465, 3965

Chakravorty S., Kembhavi A. K., Elvis M., Ferland G., 2009, MNRAS , 393, 83

Costanzo D., et al., 2022, , 659, A161

Crenshaw D. M., Kraemer S. B., Boggess A., Maran S. P., Mushotzky R. F., Wu C.-C., 1999, ApJ , 516, 750

Czerny B., 2006, in Gaskell C. M., McHardy I. M., Peterson B. M., Sergeev S. G., eds, Astronomical Society of the Pacific Conference Series Vol. 360, AGN Variability from X-Rays to Radio Waves. p. 265

De Marco B., et al., 2020, , 634, A65

Ebrero J., Kriss G. A., Kaastra J. S., Ely J. C., 2016, , 586, A72

Edelson R., Vaughan S., Malkan M., Kelly B. C., Smith K. L., Boyd P. T., Mushotzky R., 2014, ApJ , 795, 2

Elvis M., Risaliti G., Nicastro F., Miller J. M., Fiore F., Puccetti S., 2004, ApJ , 615, L25

Evans P. A., et al., 2009, MNRAS , 397, 1177

Fabian A. C., Rees M. J., Stella L., White N. E., 1989, MNRAS , 238, 729

Gallo L. C., 2011, JRASC , 105, 143

Gallo L. C., Tanaka Y., Boller T., Fabian A. C., Vaughan S., Brandt W. N., 2004, MNRAS , 353, 1064

Gallo L. C., et al., 2015, MNRAS , 446, 633

Gallo L. C., Blue D. M., Grupe D., Komossa S., Wilkins D. R., 2018, MNRAS , 478, 2557

Gallo L. C., Gonzalez A. G., Miller J. M., 2021, ApJ , 908, L33

Gehrels N., et al., 2004, ApJ , 611, 1005

George I. M., Mushotzky R., Turner T. J., Yaqoob T., Ptak A., Nandra K., Netzer H., 1998, ApJ , 509, 146

Giustini M., Proga D., 2021, in Pović M., Marziani P., Masegosa J., Netzer H., Negu S. H., Tessema S. B., eds, Vol. 356, Nuclear Activity in Galaxies Across Cosmic Time. pp 82–86 (arXiv:2002.07564), doi:10.1017/S1743921320002628

Gonzalez A. G., Wilkins D. R., Gallo L. C., 2017, MNRAS , 472, 1932

Gonzalez A. G., Gallo L. C., Miller J. M., Kammoun E. S., Ghosh A., Pottie B. A., 2024, MNRAS , 527, 5569

Grinberg V., Nowak M. A., Hell N., 2020, , 643, A109

Groves B., 2007, in Ho L. C., Wang J. W., eds, Astronomical Society of the Pacific Conference Series Vol. 373, The Central Engine of Active Galactic Nuclei. p. 511 (arXiv:astro-ph/0612309), doi:10.48550/arXiv.astro-ph/0612309

Harrison C., 2014, PhD thesis, Durham University, UK

Hickox R. C., Alexander D. M., 2018, ARA&A , 56, 625

Holt S. S., Mushotzky R. F., Becker R. H., Boldt E. A., Serlemitsos P. J., Szymkowiak A. E., White N. E., 1980, ApJ , 241, L13

Hönig S. F., 2019, ApJ , 884, 171

Jansen F., et al., 2001, , 365, L1

Kaastra J. S., et al., 2014, Science, 345, 64

Kang J.-L., Wang J.-X., Fu S.-Q., 2023, MNRAS , 525, 1941

Kara E., et al., 2015a, MNRAS , 446, 737

Kara E., et al., 2015b, MNRAS , 449, 234

Kara E., et al., 2021, ApJ , 922, 151

Krongold Y., Nicastro F., Elvis M., Brickhouse N., Binette L., Mathur S., Jiménez-Bailón E., 2007, ApJ , 659, 1022

Laha S., Guainazzi M., Dewangan G. C., Chakravorty S., Kembhavi A. K., 2014, MNRAS , 441, 2613

Laha S., Guainazzi M., Chakravorty S., Dewangan G. C., Kembhavi A. K., 2016, MNRAS , 457, 3896

Leighly K., Kunieda H., Tsusaka Y., Awaki H., Tsuruta S., 1994, ApJ , 421, 69

Longinotti A. L., et al., 2013, ApJ , 766, 104

Longinotti A. L., et al., 2019, ApJ , 875, 150

Miller L., Turner T. J., Reeves J. N., Lobban A., Kraemer S. B., Crenshaw D. M., 2010, MNRAS , 403, 196

Murray N., Chiang J., Grossman S. A., Voit G. M., 1995, ApJ , 451, 498

Nardini E., Risaliti G., 2011, MNRAS , 417, 2571

Netzer H., 2013, The Physics and Evolution of Active Galactic Nuclei

Nowak M. A., et al., 2011, ApJ , 728, 13

Panessa F., Baldi R. D., Laor A., Padovani P., Behar E., McHardy I., 2019, Nature Astronomy, 3, 387

Parker M. L., et al., 2019, MNRAS , 490, 683

Petrucci P. O., Ursini F., De Rosa A., Bianchi S., Cappi M., Matt G., Dadina M., Malzac J., 2018, , 611, A59

Petrucci P. O., et al., 2020, , 634, A85

Pier E. A., Krolik J. H., 1992, ApJ , 399, L23

Pier E. A., Krolik J. H., 1993, ApJ , 418, 673

Pottie B., Gallo L. C., Gonzalez A. G., Miller J. M., 2023, MNRAS , 525, 3633

Puccetti S., Fiore F., Risaliti G., Capalbi M., Elvis M., Nicastro F., 2007, MNRAS , 377, 607

Reynolds C. S., 1999, in Poutanen J., Svensson R., eds, Astronomical Society of the Pacific Conference Series Vol. 161, High Energy Processes in Accreting Black Holes. p. 178 (`arXiv:astro-ph/9810018`), doi:10.48550/arXiv.astro-ph/9810018

Reynolds C. S., Fabian A. C., 1995, MNRAS , 273, 1167

Ricci C., Ueda Y., Ichikawa K., Paltani S., Boissay R., Gandhi P., Stalevski M., Awaki H., 2014, , 567, A142

Risaliti G., Elvis M., Fabbiano G., Baldi A., Zezas A., Salvati M., 2007, ApJ , 659, L111

Risaliti G., et al., 2009a, MNRAS , 393, L1

Risaliti G., et al., 2009b, ApJ , 696, 160

Risaliti G., Nardini E., Elvis M., Brenneman L., Salvati M., 2011, MNRAS , 417, 178

Schartel N., Walter R., Fink H. H., Truemper J., 1996, , 307, 33

Shakura N. I., Sunyaev R. A., 1973, , 24, 337

Soldi S., et al., 2014, , 563, A57

Starling R. L. C., Siemiginowska A., Uttley P., Soria R., 2004, MNRAS , 347, 67

Steenbrugge K. C., Kaastra J. S., de Vries C. P., Edelson R., 2003, , 402, 477

Strüder L., et al., 2001, , 365, L18

Suchkov A. A., Hanisch R. J., Voges W., Heckman T. M., 2006, AJ , 132, 1475

Svoboda J., Beuchert T., Guainazzi M., Longinotti A. L., Piconcelli E., Wilms J., 2015, , 578, A96

Tan M. Y. J., Biswas R., 2012, MNRAS , 419, 3292

Tanaka Y., Boller T., Gallo L., Keil R., Ueda Y., 2004, PASJ , 56, L9

Tripathi S., Waddell S. G. H., Gallo L. C., Welsh W. F., Chiang C. Y., 2019, MNRAS , 488, 4831

Turner T. J., Reeves J. N., Braito V., Lobban A., Kraemer S., Miller L., 2018, MNRAS , 481, 2470

Walton D. J., et al., 2013, ApJ , 777, L23

Williams P. R., et al., 2018, ApJ , 866, 75

Wilson A. S., Colbert E. J. M., 1995, ApJ , 438, 62

Xu C., Livio M., Baum S., 1999, AJ , 118, 1169

Yang Q.-X., Xie F.-G., Yuan F., Zdziarski A. A., Gierliński M., Ho L. C., Yu Z., 2015, MNRAS , 447, 1692

Zackrisson E., 2005, PhD thesis, Uppsala University, Department of Physics and Astronomy

Zoghbi A., Miller J. M., Cackett E., 2019, ApJ , 884, 26

den Herder J. W., et al., 2001, , 365, L7